Low affinity integrin states have faster ligand binding kinetics than the high affinity state

Running Title: **Ligand-interaction kinetics of integrins**

Jing Li[1, 2], Jiabin Yan[1, 2] and Timothy A. Springer[1, 2] *

Affiliations

[1]Program in Cellular and Molecular Medicine, Boston Children's Hospital
[2]Department of Biological Chemistry and Molecular Pharmacology and Department of Pediatrics, Harvard Medical School, Boston, MA 02115
*Correspondence to: springer@crystal.harvard.edu

Key words: integrin α4β1/ integrin α5β1/ binding kinetics / cytoskeletal force

Abstract. Integrin conformational ensembles contain two low-affinity states, bent-closed and extended-closed, and an active, high-affinity, extended-open state. It is widely thought that integrins must be activated before they bind ligand; however, one model holds that activation follows ligand binding. As ligand-binding kinetics are not only rate limiting for cell adhesion but also have important implications for the mechanism of activation, we measure them here for integrins α4β1 and α5β1 and show that the low-affinity states bind substantially faster than the high-affinity state. On and off-rates are similar for integrins on cell surfaces and as ectodomain fragments. Although the extended-open conformation's on-rate is ~20-fold slower, its off-rate is ~25,000-fold slower, resulting in a large affinity increase. The tighter ligand-binding pocket in the open state may slow its on-rate. Low affinity integrin states not only bind ligand more rapidly, but are also more populous on the cell surface than high affinity states. Thus, our results suggest that integrin binding to ligand may precede, rather than follow, activation by "inside-out signaling".

INTRODUCTION

Integrins are a family of receptors that in all adherent cells in the body mechanically integrate the intracellular and extracellular environments and mediate cell migration and adhesion. Their α and β-subunits associate noncovalently to form an extracellular ligand-binding head and multi-domain 'legs' that connect to single-pass transmembrane and cytoplasmic domains with binding sites for cytoskeletal adaptor or inhibitory proteins (Figure 1A). Integrins populate an ensemble with three overall conformational states: the low-affinity bent-closed (BC) and extended-closed (EC) conformations and the high-affinity extended-open (EO) conformation (Figure 1A). The equilibrium between these conformational states is allosterically regulated by extracellular ligand binding, intracellular adaptor/inhibitor binding (Bouvard *et al*, 2013; Iwamoto & Calderwood, 2015) and tensile force applied by the actin cytoskeleton on the integrin β-subunit that is resisted by ligand embedded in the extracellular matrix or on cell surfaces (Kim *et al*, 2011; Legate & Fassler, 2009; Li & Springer, 2017; Nordenfelt *et al*, 2016; Park & Goda, 2016; Sun *et al*, 2016; Zhu *et al*, 2008) (Figure 1A). The EO conformation has ~1000-fold higher binding affinity for ligand than the two closed conformations and is the final competent state to mediate cell adhesion and migration (Li & Springer, 2018; Li *et al*, 2017; Schürpf & Springer, 2011). Many previous studies have emphasized the importance of force in regulating integrin adhesiveness (Alon & Dustin, 2007; Astrof *et al*, 2006; Li & Springer, 2017; Nordenfelt *et al.*, 2016; Nordenfelt *et al*, 2017; Sun *et al*, 2019; Zhu *et al.*, 2008). Recent measurements of the intrinsic ligand-binding affinity of each conformational state and the equilibria linking them enabled a thermodynamic comparison of integrin activation models (Li & Springer, 2017, 2018; Li *et al.*, 2017). Remarkably, only the combination of adaptor binding and cytoskeletal force can activate integrins in an ultra-sensitive, switch-like manner over a narrow range of signal input that is the sine qua non of cellular signaling (Kuriyan, 2012; Li & Springer,

2017). The large increase in length between the bent and extended conformations (Figure 1A) is indispensable for switch-like integrin activation.

Despite these advances, thermodynamics cannot describe the sequence of events in a multi-step transition; furthermore, energy-driven processes such as cytoskeleton movements occur under non-equilibrium conditions. To quantitatively relate the steps involved in signal transmission across the plasma membrane in integrins, ligand-binding on- and off- rates of each conformational state are of key importance. These parameters also determine whether integrin encounter of ligand is timely and whether the ligand remains bound for a sufficiently long time for the integrin to exert its function in the presence of force. Previous representative measurements (Dong *et al*, 2018; Kokkoli *et al*, 2004; Mould *et al*, 2014; Takagi *et al*, 2003) on integrin interaction with ligand have yielded kinetics on mixtures of conformational states, i.e., apparent on- and off-rates averaged over conformational states (Figure 1B left). However, the ligand-binding kinetics of individual integrin conformational states remain unknown. These kinetics must be determined (Figure 1B right) before we can understand how integrin function is regulated and how integrins work in concert with the cytoskeleton to provide traction for cell migration and firm adhesion for tissue integrity (Figure 1A).

For two classes of force-regulated adhesion molecules, each of which have a single low-affinity state and a single high-affinity state, selectins (Phan *et al*, 2006) and FimH (Yakovenko, 2015), it has been postulated that the kinetics are faster for the lower affinity state. If after binding to the low affinity state, subsequent conformational change to the high affinity state is rapid, fast ligand binding kinetics to the low-affinity state efficiently couples ligand binding to stabilization by applied force of the high-affinity state, which has a long lifetime (Yakovenko, 2015). However, the ligand binding kinetics of the states of these receptors has not yet been measured. Work from our group on integrin αVβ6 showed that removal of the hybrid domain in the αVβ6 head resulted in a 50-fold increase in affinity for ligand yet decreased the apparent on-rate of ligand binding (Dong *et al.*, 2018). However, whether this related to an increase in the population of the open conformation could not be determined due to the lack of tools to stabilize specific conformational states. There is a similar lack of measurements of state-specific ligand-binding kinetics on other Type-I single pass transmembrane receptors, many of which have both inactive and active conformations. In contrast, the field is more advanced for multipass receptors, such as the β2-adrenergic receptor in the G protein-coupled receptor family, which is stabilized by binding of intracellular G proteins in a high affinity state that has slower on- and off-rates (DeVree *et al*, 2016).

In this study, we utilized well-characterized conformation-specific Fabs (Li & Springer, 2018; Li *et al.*, 2017; Su *et al*, 2016) (Figure 1C) at saturating concentrations to stabilize integrins α4β1 and α5β1 into defined ensembles containing only one or two of the three integrin conformational states and measured the ligand-binding kinetics of each defined ensemble. Together with previously determined intrinsic ligand-binding affinities and populations of conformational states (Li & Springer, 2018; Li *et al.*, 2017), our measurements enable us to define ligand-binding kinetics intrinsic to each conformational state. For each integrin, the two closed states have indistinguishable on- and off-rates for ligands. Remarkably, the on-rate for ligand of the low-affinity closed integrin conformations is ~40-fold (α4β1) or ~5-fold (α5β1) higher than for the high-affinity EO conformation. The ~1,000-fold higher affinity of the EO conformation than the closed conformation is achieved by the ~25,000-fold lower off-rate of the EO conformation for both α4β1 and α5β1 integrins. These findings show for two representative β1 integrins that most ligand binding occurs to the bent-closed and/or extended-closed states. These measurements have important implications for the order of the steps in integrin activation.

RESULTS

Ligand-binding kinetics of intact α4β1 and α5β1 on cell surfaces. We measured binding kinetics of intact α4β1 on Jurkat cells to two fluorescently labeled ligands, a phenylureide derivative of Leu-Asp-Val-Pro (FITC-LDVP) and a fragment of vascular cell adhesion molecule (VCAM) containing its first two domains (Alexa488-VCAM D1D2) (Figure 2). Before adding ligands, cells were equilibrated with saturating concentrations of Fabs for 30 min at 22°C to stabilize specific conformational states (Li & Springer, 2018). Integrin extension, i.e. the EC and EO states, was stabilized with 4 μM 9EG7 Fab, which binds to the β1-subunit knee (Figure 2B). The EO conformation was stabilized with a combination of 4 μM 9EG7 Fab and 2 μM HUTS4 Fab; the latter binds to the interface between the βI and hybrid domains and stabilizes the EO conformation (Figure 2C). Ligand binding kinetics was monitored as mean fluorescence intensity (MFI) by flow cytometry without washing (Figure 2). Beginning at about 10 minutes, a 500-fold higher concentration of unlabeled ligand was added to measure the kinetics of dissociation. Background MFI at each fluorescent ligand concentration, measured under identical conditions except in presence of 10 mM EDTA, showed no significant difference at different time points during the association and dissociation measurements (Figure 2, 3—figure supplement 1) and was averaged across different time points and subtracted to obtain specific binding.

Under basal conditions with all three integrin states present in the ensemble, binding of FITC-LDVP to Jurkat cells reached equilibrium within 3 min (Figure 2A). Upon addition of a 500-fold excess of LDVP, dissociation of FITC-LDVP was rapid and was 99.7% complete by 5 min (Figure 2A). In contrast, both binding and dissociation of FITC-LDVP were slower when only the extended conformations (EC and EO) were present on Jurkat cells (Figure 2B). Reaching steady state required ~5 min after addition of 20 nM FITC-LDVP, ~10 min with 10 nM ligand, and was not reached after 10 min with 5 nM ligand. After 10 min of dissociation, only 19.4% of ligand had dissociated (Figure 2B). Association and dissociation were even slower when only the EO conformation was present (Figure 2C). After 15 min of association, much less ligand had bound (Figure 2C) than when both EC and EO conformations were present (Figure 2B). Dissociation was also slower, with only 1.2% of bound ligand dissociating after 10 min (Figure 2C).

VCAM D1D2 binds with ~100-fold lower affinity than LDVP to α4β1 (Figure 5 in (Li & Springer, 2018)). As a result, binding to the basal ensemble was too low to measure over the noise from unbound ligand; however, we were able to measure binding kinetics to intact α4β1 stabilized in the extended (EC+EO) and EO states (Figure 2D and E). When the two extended conformations (EC and EO) were present, binding of all three concentrations of Alexa488-VCAM D1D2 (10nM, 20nM and 30nM) reached equilibria within 2 min. Upon addition of a large excess of LDVP, dissociation of Alexa488-VCAM D1D2 was also fast; 100% dissociated by 5min (Figure 2D). Association and dissociation both became markedly slower when only the EO conformation of α4β1 was present (Figure 2E).

To address the generality of these results, we studied another integrin and cell type by measuring binding of a fluorescently-labeled two-domain fragment of fibronectin (Alexa488-$Fn3_{9-10}$) to intact α5β1 integrin on K562 cells (Figure 3). The BC conformation of α5β1 integrin on K562 cells is more stable than that of α4β1 integrin on Jurkat cells (Li & Springer, 2018). Therefore, to assure that the extended states (EC+EO) were saturably populated, they were stabilized with a combination of two Fabs, 6 μM 9EG7 Fab and 2 μM SNAKA51 Fab (schematic, Figure 3A). The EO state of α5β1was stabilized with the same combination of Fabs as used for α4β1 (Figure 3B schematic). Although binding affinity was too low to measure kinetics of the basal ensemble (Li *et al.*, 2017), we were able to measure Alexa488-$Fn3_{9-10}$ kinetics with the EC+EO and EO ensembles of intact α5β1 (Figure 3). When α5β1 was stabilized in the EO conformation, Alexa488-$Fn3_{9-10}$ bound and dissociated significantly more slowly than when both the EC and EO states of α5β1 were present in the ensemble (Figure 3A and B). Faster binding and dissociation of Alexa488-$Fn3_{9-10}$ from the EC+EO ensemble than EO showed that the EC state of α5β1 binds and dissociates faster than the EO state, just as found for α4β1.

To quantify the binding kinetics of intact α4β1 and α5β1 under each condition, we globally fit specific binding in both association and dissociation phases at each concentration of fluorescently labeled ligand to the 1 vs. 1 Langmuir binding model (lines in Figure 2A-E and 3A-B). Apparent on- and off-rates, k_{on}^{app} and k_{off}^{app}, were well fit, with low fitting errors relative to the measured values (Figure 2F and Figure 3C). The ratio of the apparent off- and on- rates, $k_{off}^{app}/k_{on}^{app}$, agrees reasonably well with the previously determined equilibrium dissociation constants shown as K_d in Figs. 2F and 3C (Li & Springer, 2018; Li *et al.*, 2017). These agreements suggest that the 1 vs. 1 Langmuir binding model can reasonably fit the kinetic data; i.e., the kinetics of conformational change between states is sufficiently fast relative to the kinetics of ligand binding to not perturb ligand binding kinetics. Thus, the relative populations of unbound states in the ensemble were not perturbed by removal by binding to ligand.

Overall, these results show that ligand binds to and dissociates from the EO conformation more slowly than from the BC and EC conformations. The kinetics measured here for the basal and EC+EO ensembles are apparent, because they include contributions from distinct conformational states present in these ensembles. In contrast, EO state kinetics are measured exactly because EO is the only state present in the EO ensemble. In the final section of Results, we will use previous measurements of the populations of the states in each ensemble to calculate the on- and off-rates for conformations within mixtures of states.

Binding kinetics of soluble α5β1 ectodomain for $Fn3_{9-10}$. We utilized bio-layer interferometry (BLI) (Wallner *et al*, 2013) to measure the kinetics of binding of an ectodomain fragment of α5β1 to the biotin-labeled $Fn3_{9-10}$ fragment of fibronectin immobilized on streptavidin biosensors (Figure 4). The ectodomain was truncated just prior to the transmembrane domains of the α5 and β1 subunits and was expressed in a cell line containing a glycan processing mutation so that it had high-mannose rather than complex-type N-glycans. Truncation of α5β1 and high mannose glycoforms substantially raises the basal population of the EO relative to that of the EO state of intact α5β1 on cell surfaces (Figure 4D and 7E in (Li *et al.*, 2017)), enabling measurement here of basal ensemble $Fn3_{9-10}$ binding kinetics.

Binding kinetics were measured by transferring $Fn3_{9-10}$ biosensors to wells containing the α5β1 ectodomain in the absence or presence of conformation-stabilizing Fabs. Dissociation kinetics were measured by transfer of sensors to wells lacking the integrin but containing identical Fab concentrations (Figure 4 A-D). Equilibrium K_d values were previously shown to be independent of the Fab used to stabilize a particular state (Figure 3 in (Li *et al.*, 2017)). However, we were concerned that binding of Fabs, particularly those that bind near ligand binding sites, might slow kinetics and therefore tested this by varying the Fabs used to stabilize the EO state.

The kinetic curves showed that the α5β1 ectodomain EO state associated more slowly than the mixtures with the closed states and also dissociated more slowly (Figure 4A-D and 4F). Overall, these differences among ensembles resembled those found for the EC+EO ensemble and EO state of intact α5β1 on K562 cells and extended measurements to the basal α5β1 ensemble. The on and off-rates of the EO state for $Fn3_{9-10}$ determined in the presence of 12G10 Fab were 4-fold and 2-fold lower, respectively, than those determined in the presence of 9EG7&HUTS4 Fabs (Figure 4C, 4D and 4F). As 12G10 Fab binds close to the ligand-binding site in the β1 domain (Figure 1A), we use k_{off}^{app} and k_{on}^{app} kinetics determined with the 9EG7, 8E3, 9EG7 & HUTS4 Fabs, which bind far from the ligand-binding site, for calculating true (k_{off} and k_{on}) kinetic rates for each state in the final section of Results.

The off-rate of the closed states. Due to the low affinities of the closed states there was too little binding to directly measure k_{on} or k_{off} in presence of saturating closure-stabilizing Fabs. We therefore used another approach. We first allowed ligand binding to integrins to reach steady state in the absence of a closure-stabilizing Fab. We then added different concentrations of closure-stabilizing Fab mAb13 and measured dissociation kinetics (Figs. 5-6). Dissociation of the ligand from the EO state is very slow as shown above and is negligible in our experimental time scale. At high Fab mAb13 concentrations, when the EO ligand-bound state (EO•L) converts to either BC•L or EC•L (grouped together here as C•L), mAb13 Fab binds and

prevents back-conversion to EO•L (Figure 5A, B). After saturating concentrations of Fab mAb13 are added to basal or EO+EC ensembles pre-equilibrated with ligand, the effective off-rate is contributed by two steps, the conformational change from EO•L to C•L and the dissociation of ligand from mAb13-bound C•L (mAb13•C•L) (Figure5A, B). Thus, the observed off-rate at saturating concentration of mAb13 Fab is contributed by the rates of both steps and permits the determination of the lower limit of k_{off}^{C}.

We measured FITC-LDVP dissociation from basal or extended ensembles of α4β1 on Jurkat cells after addition of a range of mAb13 Fab concentrations (Figure 5A-B). Saturable binding of mAb13 Fab to nascent cell surface C•L was evident from the approach to a plateau of k_{off}^{max} (Figure 5A-C). The k_{off}^{max} values measured for LDVP dissociation from basal and extended α4β1 ensembles on Jurkat cells were similar and within error of one another, with an average of ~120 $*10^{-3}$ /s (Figure 5C).

Similarly, we measured $Fn3_{9-10}$ dissociation from basal or extended ensembles of the $\alpha_5\beta_1$ ectodomain (Figure 6). The effect of mAb13 Fab on increasing k_{off} was saturable, as shown by approach to a plateau (Figure 6A-C). The fit to a saturation dose response curve yielded k_{off}^{max} values for the basal and extended ensembles of (1600 ± 100) $*10^{-3}$ /s and (1900 ± 100) $*10^{-3}$/s, respectively (Figure 6C).

Calculation of ligand-binding kinetics from ensemble measurements. We directly measured the ligand-binding and dissociation kinetics for the EO state of α4β1 and α5β1 (Figure 2C&E, Figure 3B, and Figure 4C). In contrast, kinetics for the BC and EC states were only measured within ensembles. Their kinetics are convoluted in two respects. First, measurements on ensembles contain kinetics contributed by all states within the ensemble. Second, apparent association and dissociation kinetics may each contain a contribution from the kinetics of conformational change (Figure 1B). Figure 1B left shows apparent on- and off-rates and Figure 1B right shows all the actual pathways by which ligand binding and dissociation can occur, which include all known integrin conformational states and the kinetics of conformational change between them. Furthermore, after ligand binding to the closed states, rapid conformational change to the EO state occurs and is responsible for our ability to measure the kinetics of binding as a result of accumulation of ligand-bound integrin in the EO state.

The underlying assumption for deconvoluting the kinetics of the closed states is that if integrin conformational transition kinetics (BC⇌EO, EC⇌EO, BC⇌EC, BC·L⇌EO·L, EC·L⇌EO·L, BC·L⇌EC·L) are sufficiently fast so that the populations of the three integrin states do not deviate significantly during our experiments from the equilibrium values of the populations, then measured kinetics will not be significantly limited by conformational transition kinetics. In this case, both free integrins and ligand-bound integrins can be considered as readily equilibrated among their conformational states, and ligand binding coupled with integrin conformational changes can be approximated by the apparent 1 vs. 1 reaction between integrin and ligand (this allows the double tildes in Eqs. 1-4 in Figure 7A to be treated as equal signs). All on- and off- rates measured here were well fit with the 1 vs. 1 Langmuir binding model (Figure 2A-E, Figure 3A-B, Figure 4A-D, Fig 5B-C, and Figure 6A-B), supporting this assumption. Moreover, reasonable agreement between the ratios of the apparent off- and on-rates, $k_{off}^{app}/k_{on}^{app}$, and previously determined equilibrium dissociation constants, K_d, (Figs. 2F, 3C and 4F), validates the assumption that the apparent on- and off- rates (k_{on}^{app} and k_{off}^{app}) for each defined ensemble can be approximated by the on- and off- rates of each state weighted by its population in the ensemble (Figure 7A, Eqs. 1-4). The population of the integrin states in absence of ligand (BC, EC, and EO) and in presence of saturating concentrations of ligand (BC•L, EC•L, and EO•L) were calculated based on the previously determined population and ligand-binding affinity of each state (Figure 7–figure supplement 3B, Eqs. S5-S10) in the respective integrin α4β1 and α5β1 preparations (Li & Springer, 2018; Li *et al.*, 2017) and are shown in Figure 7B.

On- and off- rates for each $\alpha_4\beta_1$ and $\alpha_5\beta_1$ integrin state on intact cells and for the purified α5β1 ectodomain are summarized in Figure 7C. Values are best determined, i.e. with the lowest

errors, for the directly determined EO state on and off-rates. Errors were higher for the BC and EC states, particularly for k_{off}. Therefore, k_{off} values for each state were also calculated from $k_{off} = K_d * k_{on}$ (Figure 7C), where K_d is from equilibrium measurements (Li & Springer, 2018; Li *et al.*, 2017). The k_{off} values of each state determined from these two strategies agree well with one another for each integrin-ligand pair. We do not report in Figure 7C the lower limit of k_{off}^{C} and k_{off}^{EC} approached by measuring dissociation in presence of a closure-stabilizing Fab in Fig, 5 and 6; however, these values were comparable to those calculated from measurements on ensembles as described in this section or calculated from $k_{off} = K_d * k_{on}$.

DISCUSSION

Strengths and limitations of different approaches to studying integrin conformational states Employing conformation-specific Fabs against the integrin β1 subunit to stabilize integrins into defined ensembles, we determined the on- and off-rates of each integrin conformational state. The conformational specificities of these Fabs were determined with negative stain EM (nsEM) with the integrin α5β1 ectodomain (Su *et al.*, 2016) and further verified by ligand binding affinity measurements in presence of saturating concentrations of Fab (Li *et al.*, 2017). In the latter study, we used between two to four independent antibodies or antibody combinations, often binding to distinct domains, to stabilize α5β1 ectodomain ensembles containing the EO, EC, EO+EC, and EC+BC states. In all cases, independent antibodies that stabilized the same conformational state(s) as determined by EM yielded similar ensemble *K*d values (Figure 3 in (Li & Springer, 2018; Li *et al.*, 2017), validating stabilization of the same state(s), and supporting the assumption that these states resembled those in the absence of Fab. Quantitatively, the antibodies must be highly state-specific in order to give large shifts in affinities, to give consistent intrinsic affinities on constructs with large differences in basal affinities, and to give similar intrinsic affinities using Fabs to distinct epitopes. The conformational specificity of these antibodies and their use at sufficient concentration to saturate these states are important for our previous thermodynamic studies {Li, 2017 #24745) and the current kinetic study.

To prevent confusion, we should discuss a recent elegant cryoEM structure of intact integrin α5β1 in nanodiscs bound both to TS2/16 Fv-clasp and $Fn3_{7-10}$ that showed for the first time that α5β1 recognizes both the RGD motif in Fn3 domain 10 and the synergy site in Fn3 domain 9 of fibronectin (Schumacher *et al*, 2021). In a contrast to the antibodies used here, TS2/16 antibody, which originated in our laboratory (Figure 1, lane 36 (Sanchez-Madrid *et al*, 1982)), is stimulatory but not conformation specific. We previously found that TS2/16 Fab can bind all three states of the α5β1 ectodomain, BC, EC, and EO, as shown by nsEM (Figure 4C of (Su *et al.*, 2016). Saturating 3 μM TS2/16 Fab stabilized some $Fn3_{9-10}$ binding to cells, but far less than the open-stabilizing Fabs 12G10 and HUTS4 (Figure 6A of (Su *et al.*, 2016)). Overall, these results suggest that TS2/16 Fab binds to both the EO and BC+EC states but has higher affinity for the EO state. Binding to both open and closed conformations was confirmed by cryo-EM and crystal structures that showed that TS2/16 Fv-clasp can bind both the open (PDB ID 7NWL) and closed (7CEB) conformations of β1 integrins (Arimori *et al*, 2021; Schumacher *et al.*, 2021). Because of its lack of state specificity, we have never used TS2/16 to stabilize a specific integrin conformational state.

It is common in cryoEM and nsEM to form complexes in a large excess of one or more components, and then separate the complex from free components by gel filtration. During gel filtration and up until cryo-cooling or fixation by negative stain, complexes will dissociate because the law of mass action requires free components to stabilize complex formation, as defined by $[I \bullet L] = ([I] \cdot [L])/K_d$ where I and L are integrin and ligand, respectively. Stabilizing integrins $\geqslant$99% in the desired conformations in this study required the use of Fabs at concentrations 80 fold higher than their EC50 values for each integrin preparation (Tables S1 in (Li & Springer, 2018; Li *et al.*, 2017)). For stabilizing intact α4β1 and α5β1 in extended and open states, some Fab EC50 values are in the hundreds of nM range, which required a combination

of two compatible Fabs to conserve protein supplies. Compared to the integrin that was being stabilized here, Fabs were used at molar excesses ranging from 9 to 48,000-fold. This contrasts to the 1:1 ratio in integrin complexes isolated from free components for ns and cryoEM. Such complexes are out of equilibrium and must dissociate, the rate and extent of which are governed by the kinetics and equilibria such as measured here and previously, respectively (Li & Springer, 2018; Li *et al.*, 2017).

Conformational equilibria of the α5β1 ectodomain determined with $Fn3_{9\text{-}10}$ and RGD peptides as ligands were similar (Figure 4 in (Li *et al.*, 2017); which makes it important to note that the claim that RGD, because it lacks the synergy site, cannot stabilize α5β1 headpiece opening, was not supported by cited articles (Schumacher *et al.*, 2021). Addition of 1 mM RGD peptide to the α5β1 headpiece resulted in the presence of the headpiece in both the open and closed conformations as shown by nsEM (Figure 2B in (Takagi *et al.*, 2003)). At saturating concentrations of ligands, integrin preparations vary in the percentage of ligand that is bound to each state (Figure 7B and see Figure 7–figure supplement 3 for a wide range of integrin preparations). The α5β1 headpiece used in (Takagi *et al.*, 2003) is ~50% open when saturably bound to a cyclic RGD peptide, in agreement with the nsEM results. The failure to open of the closed α5β1 headpiece in crystals soaked with RGD was to be expected because the lattice contacts frustrated opening and in one publication a closed state-specific Fab was also bound (Nagae *et al*, 2012; Xia & Springer, 2014). In recent unpublished work, we found that while Mn^{2+} increases population of the EO state of cell surface α5β1, the large majority remains in the BC state (Anderson, Li, and Springer), in excellent agreement with the predominance of the BC state in Mn^{2+} in α5β1 in nanodiscs (Schumacher *et al.*, 2021). Additionally, while α5β1 is less bent than some other integrins (Schumacher *et al.*, 2021; Su *et al.*, 2016), it still has distinct bent and extended conformations and it remains appropriate to describe α5β1 as having a BC state.

Intrinsic ligand-binding kinetics of integrin conformational states. The advance in this study is the measurement of ligand binding and dissociation kinetics of integrin conformational states for the first time. Furthermore, we have made the surprising observation that the low affinity integrin BC and EC states have faster on-rates than the high affinity EO state. While we compare k_{off}/k_{on} to previously determined equilibrium K_d values, that is only to demonstrate that the values we have determined are not affected by slow equilibration among the conformational states, which would have invalidated our assumption that the apparent ligand binding kinetics are the composites of the ligand binding kinetics of each state at equilibrium.

Previous studies on α4β1 and α5β1 integrins showed that their affinities were intrinsic to the type of integrin, the ligand, and the state; i.e., independent of the type of integrin preparation: cell surface, soluble ectodomain or headpiece, or N-glycosylation status (Li & Springer, 2018; Li *et al.*, 2017). Similar to intrinsic affinities, the results here on ligand-binding kinetics were consistent with on-rates and off-rates that are intrinsic to integrin conformational states. On-rates for fibronectin $Fn3_{9\text{-}10}$ binding to EO states of intact α5β1 on cell surfaces and the α5β1 ectodomain were identical and off-rates differed by only 1.8-fold. Similarly, on- and off-rates for the EC state of the intact cell-surface and ectodomain forms of α5β1 differed only by 1.1-fold and 1.9-fold respectively. Moreover, BC and EC states for both types of integrins had similar kinetics, showing that ligand binding on and off-rates were determined by whether the headpiece was closed or open, and not by extension. These findings are in agreement with the essentially identical intrinsic affinities of the two closed states (Li & Springer, 2018; Li *et al.*, 2017). In further agreement, crystal structures of the integrin αIIbβ3 ectodomain in the BC state and of the αIIbβ3 closed headpiece fragment, which has no interactions with the lower legs and thus serves as a model for the EC conformation (Zhu *et al.*, 2008; Zhu *et al*, 2013), show essentially identical conformations of the ligand binding site.

We checked whether kinetics might be influenced by bound Fabs, in contrast to equilibria, which showed no dependence (Li *et al.*, 2017). Among two Fabs used to stabilize the EO state, ligand association and dissociation was slower with 12G10, which binds near the

ligand binding site in the βI domain than with HUTS4, which binds distally in the hybrid domain (Figure 4F). As Fabs generally decrease dynamic protein motions in their epitopes (Wei *et al*, 2014) and may also sterically slow binding, the kinetics measured using HUTS4 Fab more likely approximate integrin kinetics in the absence of Fab and are reported in Figure 7C.

The kinetics of the EC and BC states were calculated from measurements on extended or basal ensembles after correction for the kinetics in these ensembles contributed by the EO state. As a check on these measurements, we also measured k_{off} in the presence of mAb13 Fab, which after conformational conversion of EO•L to EC•L+BC•L, trapped the closed states so that their dissociation could be measured. The lower limit of k_{off}^{C} and k_{off}^{EC} determined from these experiments (Figure 5C and 6C) are in good agreement with off-rates of the closed states calculated from ensembles and also from $K_d \cdot k_{off}$ (Figure 7C).

Typical protein-protein on-rates as found for antibody-antigen interactions are in the range of 10^5 to 10^6 M^{-1} s^{-1} (Alsallaq & Zhou, 2008). The on-rates for the BC and EC states were in this range. In contrast, the on-rates for EO states for the corresponding integrin-ligand pairs were slower and suggest a hindrance to ligand binding. The open conformation of integrins has a tighter ligand-binding pocket around the metal ion-dependent adhesion site (MIDAS) than the closed state (Dong *et al*, 2017; Nagae *et al.*, 2012; Schumacher *et al.*, 2021; Xia & Springer, 2014; Xiao *et al*, 2004; Zhu *et al.*, 2013) (Figure 7D). Movement of the β1-α1 loop toward the ligand and the MIDAS Mg^{2+} ion upon βI domain opening partially buries the Mg^{2+} ion and is expected to slow binding of the Asp sidechain, which must fit into a tight pocket with a specific geometry dictated by partially covalent and highly directional Asp sidechain metal coordination and hydrogen bonds to the β1-α1 loop backbone amide nitrogens.

The ~1,000-fold higher affinities of the EO than the closed conformations for both α4β1 and α5β1 integrins are achieved by the ~25,000-fold slower off-rate of the EO conformation (Figure 7C). Similar to the differences in on-rates, the differences in off-rates can be understood in terms of the structural details in the ligand-binding pocket and the much higher affinity of the EO state. The tighter Asp sidechain binding pocket and greater burial of the Asp provide a barrier to dissociation (Figure 7D). The number of hydrogen bonds of the Asp sidechain to the β1-α1 loop backbone increases in the open state (Zhu *et al.*, 2013). Furthermore, the greater burial of these polar bonds and increased network of hydrogen bonds around them increases their strength.

The intrinsic ligand-binding kinetics of integrin conformational states described here are consistent with previous kinetic observations. These studies showed that activating integrin ensembles with Mn^{2+} or activating IgG or Fab, using conditions that in retrospect would partially but not completely shift integrin ensembles to the EO state, decreased the ligand off-rates of integrins α4β1 and α5β1 (Chigaev *et al*, 2001; Takagi *et al.*, 2003). The extremely long lifetime of the α5β1 complex with fibronectin in the EO state, around several hours, also explains why the α5β1 complex with fibronectin in Mn^{2+} was much more rapidly reversed by mAb 13 IgG specific for the closed conformations than by competitive inhibitor (Mould *et al*, 2016; Mould *et al.*, 2014). One important difference from most previous work, including our own (Takagi *et al.*, 2003), is our ability to fit all of our data to a 1:1 binding model. All our fits were global; i.e., data at all ligand concentrations were used to create the fits in each panel shown in figures. This is the most rigorous way to fit data. When more variables are introduced such as a rate for conformational change to a different state or additional binding and dissociation rates, better fits can always be achieved. Notably, our data fit the 1:1 binding model whether one, two, or three states were present in the ensemble. Therefore, we believe that the rates of interconversion are relatively fast and attribute the difference from some previous results to homogenous protein preparations free from aggregates and homogenous incorporation of binding partners either as native proteins on intact cells or as purified proteins immobilized uniformly through single, site-specific biotins to streptavidin biosensors.

Integrin activation. A major impetus for these studies was to determine the pathway for activation of integrins in cells, i.e. the activation trajectory. Of key importance is how integrins on the cell surface first engage ligands. Integrin signaling is governed by cytoskeletal force and the

force-stabilized, high-affinity, extended-open conformation is the only state competent to mediate cell adhesion (Alon & Dustin, 2007; Astrof *et al.*, 2006; Li & Springer, 2018; Li *et al.*, 2017; Nordenfelt *et al.*, 2016; Nordenfelt *et al.*, 2017; Sun *et al.*, 2019; Zhu *et al.*, 2008). Mechanotransduction occurs when an integrin binds to ligand anchored in the extracellular environment and at the same time its cytoplasmic domain binds to a cytoskeletal adaptor and links to actin retrograde flow, resulting in a tensile force transmitted through the integrin that stabilizes the extended-open conformation over the bent-closed conformation. Thus the on- and off- rates of ligand binding to integrins are among the key parameters that determine the efficiency of cytoskeletal force regulation. We found that the closed states, with loose ligand binding pockets, have higher on-rates for ligand binding, making them the most efficient state for encountering ligand.

What is the cell biological context in which we should think about our finding that the closed states are kinetically poised to bind ligand as the first extracellular event in integrin activation? And what is integrin inside-out signaling? This term was first used in a review on adhesion molecules of the immune system (Springer, 1990) after the discovery that integrins on lymphocytes (Dustin & Springer, 1989) and platelets (reviewed in (Hynes, 1992)) only became active in adhesion after these cells were stimulated through other receptors. The commonality is that lymphocytes and platelets in the bloodstream do not exhibit polarization or actin retrograde flow, but do so after stimulation, consistent with the model that integrins are activated by the tensile force transmitted through them between actin retrograde flow and extracellularly embedded ligands (Li & Springer, 2017) and findings that integrins are aligned with actin retrograde flow (Nordenfelt *et al.*, 2017; Swaminathan *et al*, 2017) and transmit tensile force (Nordenfelt *et al.*, 2016; Sun *et al.*, 2016). Our results on the kinetics of ligand binding of different integrin conformational states are relevant to both integrins on cells in suspension as studied here and to unbound integrins on adherent cells, since the kinetics are intrinsic to the EO, EC, and BC states.

Our results on ligand-binding kinetics provide a stepping stone to a remaining important question, the kinetics of integrin conformational change. Equilibria show that the ligand-bound open state is ~1,000 fold more favored than the ligand-bound closed state. Thus following step 1 of binding of ligand to the closed state, step 2 of conformational change to the more stable ligand-bound EO state should be rapid, but remains to be measured.

It should be emphasized that the populations of integrin conformational states we have measured on cells in suspension are for unliganded integrins. On adherent cells, integrins bound to ligand on the substrate belong to a separate pool of liganded integrins, which are removed from and not included in the populations of unliganded integrins we have measured. Ligand-bound integrins may dominate on the ventral surface of adherent cells, as emphasized by the predominance of extended integrin LFA-1 on the ventral surface of lymphoid cells bound to the LFA-1 ligand ICAM1, and the greater abundance of bent LFA-1 on the ventral surface of the same cells bound to the α4β1 ligand fibronectin (Moore *et al*, 2018).

Are the populations of unliganded integrin conformational states the same on suspended and adherent cells? We do not know the kinetics of binding of adaptors such as talin or kindlin to integrins or what fraction of unliganded integrins on suspended and adherent cells are bound to adaptors. The adaptor talin appears to interfere with association between integrin α and β subunit transmembrane/cytoplasmic domains in the BC state (Lau *et al*, 2009; Zhu *et al*, 2009), and thus if talin is bound to a higher proportion of unliganded integrins in adherent cells than suspended cells, the populations of unliganded EC and EO states might be increased relative to the BC state. Adaptor-bound unliganded integrins might also show preferential localizations in cells. Extended and unliganded β1 integrins have been shown to localize along the leading edge of fibroblast lamellae and growth cone filopodia to probe for adhesion sites (Galbraith *et al*, 2007). High affinity, unliganded integrin αVβ3 was also shown to be recruited to lamellipodia in endothelial cell migration (Kiosses *et al*, 2001). Rapid ligand binding, together with rapid cytoskeletal adaptor binding, would enable their coincidence to regulate integrin activation, thus

providing a seamless method for activating integrins at cellular locations where actin, talin, and kindlin are activated and extracellular ligand is available.

MATERIALS AND METHODS

Fabs. IgGs, 8E3 (Mould *et al*, 2005), 9EG7 (Bazzoni *et al*, 1995), 12G10 (Mould *et al*, 1995), HUTS4 (Luque *et al*, 1996), mAb13 (Akiyama *et al*, 1989) and SNAKA51 (Clark *et al*, 2005) were produced from hybridomas and purified by protein G affinity; Fabs were prepared with papain digestion in PBS (phosphate-buffered saline with 137 mM NaCl, 2.7 mM KCl, 10 mM Na2HPO4 and 1.8 mM KH2PO4, pH7.4) with 10 mM EDTA and 10 mM cysteine and papain: IgG mass ratio of 1:500 for 8 hrs at 37°C, followed by Hi-Trap Q chromatography in Tris-HCl pH 9 with a gradient in the same buffer to 0.5 M NaCl. These conformation specific Fabs are used to stabilize integrin α4β1 and α5β1 into ensembles of defined conformational states. To ensure saturable population of target conformations, conformation-specific Fabs were used at concentrations (shown in Figure legends) well above the concentration giving half-maximum responses, i. e. their EC50 values on each integrin preparation (Tables S1 in (Li & Springer, 2018; Li *et al.*, 2017)).

Integrin α5β1 soluble preparations. Integrin α5β1 ectodomain (α5 F1 to Y954 and β1 Q1 to D708) with secretion peptide, purification tags, and C-terminal clasp (Takagi *et al*, 2001) were produced by co-transfecting the pcDNA3.1/Hygro(-) vector coding the α-subunit and pIRES vector coding the β-subunit into HEK 293S GnTI$^{-/-}$ (*N*-acetylglucosaminyl transferase I deficient) cells. Stable transfectants were selected with hygromycin (100 μg/ml) and G418 (1 mg/ml), and proteins were purified from culture supernatants by His tag affinity chromatography and Superdex S200 gel filtration after cleavage of C-terminal clasp and purification tags with Tev protease (Li *et al.*, 2017).

Peptidomimetic and macromolecule fragments. FITC-conjugated α4β1 specific probe, 4-((N′-2-methylphenyl)ureido)-phenylacetyl-L-leucyl-L-aspartyl-L-valyl-L-prolyl-L-alanyl-L-alanyl-L-lysine (FITC-LDVP) and its unlabeled version, LDVP, were from Tocris Bioscience (Avonmouth, Bristol, United Kingdom). Human VCAM D1D2 (mature residues F1 to T202) were expressed and purified from HEK 293S GnTI$^{-/-}$ cell line supernatants by affinity chromatography and gel filtration (Yu *et al*, 2013). VCAM D1D2 was fluorescently labeled with Alexa Fluor 488 NHS Ester (ThermoFisher Scientific). Human $Fn3_{9\text{-}10}$ S1417C mutant (mature residues G1326 to T1509) and its synergy and RGD sites (R1374A&P1376A&R1379A&S1417C&Δ1493-1496) mutated inactive version were expressed in *E. coli* and purified as described (Li *et al.*, 2017; Takagi *et al.*, 2001). $Fn3_{9\text{-}10}$ S1417C mutant was fluorescently labeled with Alexa Fluor 488 C5 maleimide (ThermoFisher Scientific) at residue Cys-1417. Both $Fn3_{9\text{-}10}$ S1417C mutant and its inactive version were biotinylated with Maleimide-PEG11-Biotin at residue 1417 (ThermoFisher Scientific) in PBS.

Cell lines. Jurkat and K562 cell lines are purchased from ATCC, which have been authenticated by STR profiling. Monthly mycoplasma contamination tests carried out in our lab confirmed the cells in use are free of mycoplasma.

Quantitative fluorescent flow cytometry. Jurkat and K562 cells (10^6 cells/mL in RPMI-1640 medium, 10% FBS) were washed twice with assay medium (Leibovitz's L-15 medium, 10 mg/mL BSA) containing 5 mM EDTA, twice with assay medium alone, and suspended in assay medium. Cells at 2×10^6 cells/mL were incubated with indicated concentration of Fabs for 30min at 22°C. Addition of FITC-LDVP, Alexa488- VCAM D1D2 (1.6 labeling ratio) or Alexa488-$Fn3_{9\text{-}10}$ (1.0 labeling ratio) at indicated concentrations initiated association. Association was measured as mean fluorescence intensity (MFI) at successive time points after addition of the fluorescent

ligands. Addition of 500-fold higher concentration of the unlabeled ligand at the end of the association phase initiated the dissociation phase. Background MFI for FITC-LDVP, Alexa488-VCAM D1D2 and Alexa488-$Fn3_{9-10}$ in presence of 10 mM EDTA was subtracted (Figure 2, 3–figure supplement 1).

Fitting flow cytometry and BLI kinetic binding traces with 1 vs. 1 Langmuir binding model Kinetic traces including both the association phase and the dissociation phase at different analyte concentrations were globally fitted to the following function.

$$R_t=\left(\frac{1}{2}+\frac{(t_D-t)}{2|t_D-t|}\right)\frac{R_{max}k_{on}[A]}{k_{off}+k_{on}[A]}\left(1-e^{-(k_{off}+k_{on}[A])\,t}\right)$$
$$+\left(\frac{1}{2}-\frac{(t_D-t)}{2|t_D-t|}\right)\frac{R_{max}k_{on}[A]}{k_{off}+k_{on}[A]}\left(1-e^{-(k_{off}+k_{on}[A])\,t_D}\right)e^{-k_{off}(t-t_D)},$$

where t is time, R_t is response at time t, t_D is the time that dissociation starts, [A] is the analyte concentration, and R_{max} is the maximum response. The first term fits the data in the association phase and the second term fits the data in the dissociation phase. The prefactor of the first term is 1 prior to t_D and becomes 0 after t_D; whereas the prefactor for the second term is 0 prior to t_D and becomes 1 after t_D. Nonlinear least square fit of R_t, [A], and t to the above equation yields the on-rate, k_{on}, off-rate, k_{off}, and R_{max}.

Bio-Layer Interferometry (BLI). Binding kinetics of unclasped high-mannose α5β1 ectodomain and $Fn3_{9-10}$ was measured by BLI (Wallner *et al.*, 2013) with streptavidin biosensors on an Octet RED384 System. The reaction was measured on 96 well plate (200 µL/well) in buffer with 20 mM Tris HCl (pH 7.4), 150mM NaCl, 1mM Ca^{2+}, 1mM Mg^{2+} and 0.02% Tween20. Streptavidin biosensors were hydrated in reaction buffer for 10 min before starting the measurements. Each biosensor was sequentially moved through 5 wells with different components: (1) buffer for 3 minutes in baseline equilibration step; (2) 35 nM biotin-$Fn3_{9-10}$ for 1 minute for immobilization of ligand onto the biosensor; (3) indicated concentrations of Fabs for 5 minutes for another baseline equilibration; (4) indicated concentrations of α5β1 ectodomain and Fabs for the association phase measurement; (5) indicated concentrations of Fabs for the dissociation phase measurement. Each biosensor has a corresponding reference sensor that went through the same 5 steps, except in step 2 the ligand was replaced with 35 nM inactive version of $Fn3_{9-10}$ with both the RGD binding site and the synergy site (PHSRN) mutated. Background subtracted response in both the association and dissociation phases, and at different α5β1 ectodomain concentrations, were globally fit to the 1 vs. 1 Langmuir binding model, with k_{on}^{app} and k_{off}^{app} as shared fitting parameters and maximum response (R_{max}) for each biosensor as individual fitting parameter. The equilibrium binding (response) was calculated from k_{on}^{app} and k_{off}^{app} values at each each α5β1 ectodomain concentration and fit to a dose response curve to calculate K_d values as a check on $k_{off}^{app}/k_{on}^{app}$ values. To calculate equilibrium response (R_{eq}), fitted k_{on}, k_{off}, and R_{max} values at each α5β1 ectodomain concentration [A] were used to calculate R_{eq} at a time 1,000-folder longer than the "binding time", i.e., t = $1000*\frac{1}{k_{on}[A]}$, with the following equation:

$$R_{eq}=\frac{R_{max}k_{on}[A]}{k_{off}+k_{on}[A]}\left(1-e^{-(k_{off}+k_{on}[A])\,t}\right)$$

Calculating ligand-binding and dissociation rates for the BC and EC states The measured on- and off- rates (k_{on}^{app} and k_{off}^{app}) for each defined ensemble containing 2 or 3 states shown in Figs. 2-4 was approximated by the on- and off- rates of each state weighted by its population in the ensemble (Figure 7A, Eqs. 1-4). At steady state, the population of the free integrin states and the ligand-bound integrin states were calculated based on the previously determined population and intrinsic ligand-binding affinity of each state (Figure 7–figure supplement 3, Eqs. S5-S10) in the respective integrin α4β1 and α5β1 preparations (Li &

Springer, 2018; Li *et al.*, 2017) (Figure 7B). Specifically, $\frac{K_a^{EO}}{K_a^{EC}}$ and $\frac{K_a^{EO}}{K_a^{BC}}$ (in Figure S3B, Eqs.S8-S10), are the intrinsic ligand-binding affinity ratios of the EO state and the closed states. For integrin α4β1, the ratios were averaged to 729±211 from six α4β1 preparations, including α4β1 headpiece with high-mannose N-glycans, α4β1 ectodomain with high-mannose N-glycans, α4β1 ectodomain with complex N-glycans, and intact α4β1 on three different cell lines (Li & Springer, 2018); for integrin α5β1, the intrinsic ligand-binding affinity ratio of the EO state and the closed states were averaged to 3106 ±1689 from eight soluble α5β1 preparations that varied in presence or absence of the lower legs, of a loose clasp in place of the TM domain, and in whether the N-linked glycan was complex, high mannose, or shaved (Li *et al.*, 2017). Using k_{on}^{EO} and k_{off}^{EO} rates experimentally measured in Figs. 2-4, k_{on}^{EC} and k_{off}^{EC} were derived from the $k_{on}^{app(EC+EO)}$ and $k_{off}^{app(EC+EO)}$ measured in extended ensembles, respectively (Figure 7A, Eqs.1-2). By including the values for k_{on}^{EC} and k_{off}^{EC} in addition to k_{on}^{EO} and k_{off}^{EO}, k_{on}^{BC} and k_{off}^{BC} were then derived from $k_{on}^{app\,(BC+EC+EO)}$ and $k_{off}^{app\,(BC+EC+EO)}$ measured in basal ensembles, respectively (Figure 7A, Eqs. 3-4).

Acknowledgements. We thank Kelly L. Arnett in Center for Macromolecular Interactions of Harvard Medical school for training and consultation on BLI measurement. We thank Taekjip Ha for suggestions on our manuscript. This work was funded by NIH R01 HL131729 (“Activation trajectories of integrin a5b1”).

Conflict of Interest Statement. The authors declare no competing financial interests.

Figure Legends

Figure 1. Ligand-interaction kinetics of integrin ensembles. (A) Three overall integrin conformational states (Luo *et al*, 2007). Individual domains are labeled next to the extended-open state. The structural motifs that move during opening (α1-helix, α7-helix and β6-α7 loop) are labeled in the βI domain of the EC and EO state. F represents tensile force exerted across ligand–integrin–adaptor complexes by the cytoskeleton and resisted by immobilized ligand. **(B)** Reaction scheme showing the apparent 1 vs. 1 kinetics of integrin and ligand binding (left) and the scheme taking into account conformational change (right). (**C**) Fabs utilized in this study, the integrin domains they bind, and their conformational specificity.

Figure 2. Binding kinetics of ligands to intact α4β1 on Jurkat cells. (**A-E**) Binding and dissociation of FITC-LDVP (A-C) and Alexa488-VCAM D1D2 (D-E) to α4β1 on Jurkat cells measured by flow cytometry. Cartoons in panel A, B, and C show the schemes for measuring k_{on} in the association phase and k_{off} in the dissociation phase in the basal ensemble (A), the extended ensemble stabilized with Fab 9EG7 (8 μM) (B and D), and the open ensemble stabilized with Fabs 9EG7 (4 μM) and HUTS4 (2 μM) (C and E). Specific MFI with the MFI in EDTA (Figure 2, 3–figure supplement 1) subtracted is shown as open (association) or filled (dissociation) symbols; fits are shown as thin lines. **(F)** Tabulation of results. k_{on}^{app} and k_{off}^{app} are from global fits of data at all ligand concentrations. $\frac{k_{off}^{app}}{k_{on}^{app}}$ is also shown and compared to the equilibrium K_d measurements shown in Figure4A and 4D of our previously work (Li & Springer, 2018), except for Alexa488-VCAM D1D2 binding to extended states, which was measured here (Figure 2–figure supplement 2). Errors for K_d values are SD from three independent experiments. Kinetic constants were determined multiple times. Kinetic constants determined in a preliminary experiment were used to determine the range of concentrations and times used in the experiment shown. Each of the three concentrations in the experiment shown is an independent experiment capable of determining the reported kinetics. By globally fitting kinetic constants to all three analyte concentrations, we obtained single on and off rates that combine the measurements in the three independent determinations and at the same time report errors in concentrations used and model assumptions about concentration dependence. Errors for k_{on}^{app} and k_{off}^{app} values are standard error (SE) from global nonlinear least square fitting of data at all ligand concentrations. From SE, the 95% confidence interval for the fitting parameter can be computed as [fitting value – 2*SE, fitting value + 2*SE]. Errors for $\frac{k_{off}^{app}}{k_{on}^{app}}$ are propagated from errors of k_{on}^{app} and k_{off}^{app}.

Figure 2, 3–figure supplement 1. Background binding of fluorescent ligands in presence of 10 mM EDTA. Mean fluorescent intensity (MFI) of FITC-LDVP (A) or Alexa488-VCAMD1D2 (B) on Jurkat cells and Alexa488-Fn39-10 on K562 cells (C) was recorded before and after adding an excess of unlabeled ligand in presence of 10 mM EDTA.

Figure 2–figure supplement 2. Binding of Alexa488-VCAM D1D2 to Jurkat cells under extension-stabilizing Fabs monitored by FACS. Jurkat cells at 2 million/mL were incubated with indicated concentrations of Alexa488-VCAMD1D2 and 4 μM 9EG7 Fab in L15 medium with 1% BSA for 1 hour at 22°C, and then subjected to flow cytometry without washing. Binding was measured as MFI; background MFI was determined under the same condition with 10 mM EDTA present. Data were fitted to dose response curve to determine the Kd value; error represents the standard error from the nonlinear least square fit.

Figure 3. Binding kinetics of Alexa488-Fn3$_{9\text{-}10}$ to α5β1 on K562 cells. (A-B) Binding of Alexa488-Fn3$_{9\text{-}10}$ to α5β1 on K562 cells measured by flow cytometry. Measurements were on integrins in extended ensembles (EC+EO states) in presence of Fabs 9EG7 (6 μM) and SNAKA51 (2 μM) (A) or in the open (EO state) in presence of Fabs 9EG7 (6 μM) and HUTS4 (2 μM) (B), as illustrated in the cartoons. MFI with background in EDTA subtracted (Figure 2, 3–figure supplement 1) is shown as symbols and fits are shown as lines; the association phase

has open symbols and solid lines, and the dissociation phase has filled symbols and dashed lines. (**C)** Tabulation of results. Details about experimental repeats and kinetic parameter uncertainty, including errors and confidence intervals are as described in Figure 2 legend. $k_{off}^{app}/k_{on}^{app}$ is also shown with propagated error and compared to equilibrium K_d measurements shown in Figure 7B of our previous study (Li *et al.*, 2017).

Figure 4. Binding kinetics of α5β1 ectodomain to Fn3$_{9-10}$. (A-D) Binding of unclasped high-mannose α5β1 ectodomain measured with BLI. Schemes for measuring ligand binding and dissociation in the association phase and dissociation phase are shown in each panel. α5β1 ectodomain (analyte) at the indicated concentrations in nM was bound to biotin- Fn3$_{9-10}$ immobilized on streptavidin biosensors without Fab (**A**), with 2 μM Fab 8E3 (**B**), with 2 μM 9EG7 and 5 μM HUTS4 Fabs (**C**), or with 1 μM Fab 12G10 (**D**). Arrows mark the start of the dissociation phase. Response curves are in gray and fitting curves in black. (**E**) The equilibrium binding (response) was calculated from k_{on}^{app} and k_{off}^{app} values at each α5β1 ectodomain concentration and fit to a dose response curve to calculate K_d values. These values serve as a check on the $k_{off}^{app}/k_{on}^{app}$ values in F. (**F)** k_{on}^{app} and k_{off}^{app} values from nonlinear least square fit of data in Panel A-D and K_d values from equilibrium response analysis in Panel E with 1 vs. 1 Langmuir binding model, and $k_{off}^{app}/k_{on}^{app}$ values. Errors without * for k_{on}^{app}, k_{off}^{app} and K_d are SE from nonlinear least square fits with single $k_{on}^{app}$and k_{off}^{app} as global parameters fitting to all analyte concentrations. Details about experimental repeats and uncertainties for $k_{on}^{app}$and k_{off}^{app}, including errors and confidence intervals are as described in Figure 2 legend. Errors for $k_{off}^{app}/k_{on}^{app}$ are propagated from errors of k_{on}^{app} and k_{off}^{app}. Errors with * are difference from the mean of two measurements at the same concentrations of α5β1 ectodomain from two independent purifications.

Figure 5. Dissociation of FITC-LDVP from α4β1 on Jurkat cells in presence of closure-stabilizing Fab. (**A-B)** FITC-LDVP dissociation from basal or extended ensembles of intact α4β1 on Jurkat cells measured using flow cytometry. FITC-LDVP (20nM) was incubated with Jurkat cells in absence (A) or in presence of extension-stabilizing Fab 9EG7 (4 μM) (B) for 10 minutes to reach steady state. Then, 10 μM unlabeled LDVP together with indicated concentrations of mAb13 Fab were added. Observed MFI (MFI_{obs}) values as a function of time at indicated mAb13 Fab concentrations were globally fitted to $MFI_{obs}=MFI_0*e^{-k_{off}^{app}\cdot t}+MFI_{background}$, with *MFI* at the start of dissociation (MFI_0) and background *MFI* ($MFI_{background}$) as shared parameters and k_{off}^{app} as the individual fitting parameter at each mAb13 Fab concentration. (**C**) Dependence of k_{off}^{app} on mAb13 Fab concentration. k_{off}^{app} at each mAb13 Fab concentration in panels A and B were fitted to dose response curves to determine the maximum off-rate at saturating mAb13 Fab concentration, k_{off}^{max}, and the mAb13 Fab concentration when the off-rate reaches half of the maximum, EC_{50}^{mAb13}. Experiments in panels A and B were carried out twice, first with 0, 1, 2, and 4 μM mAb13 Fab for 120 s, and then with the conditions shown, with similar k_{off}^{app} values in each experiment. All errors are SE from nonlinear least square fits.

Figure 6. Dissociation of α5β1 ectodomain from biotin- Fn3$_{9-10}$ in presence of closure-stabilizing Fab. (**A-B**) Unclasped high-mannose α5β1 ectodomain dissociation from biotin-Fn3$_{9-10}$ immobilized on streptavidin biosensors was monitored by BLI. Reaction schemes are illustrated in each panel. 50 nM α5β1 ectodomain was incubated with biotin-Fn3$_{9-10}$ biosensors for 10 minutes to reach steady state binding in absence (A) or presence of 2μM 9EG7 Fab (B). Biosensors were then transferred into wells lacking the α5β1 ectodomain in presence or absence of 9EG7 Fab as before and also containing the indicated concentrations of mAb13 Fab for measurement of dissociation. The observed response (R_{obs}) at each mAb13 Fab concentration as a function of time was individually fitted to the single exponential, $R_{obs}=R_0*e^{-k_{off}^{app}\cdot t}$, for the initial response at the start of dissociation (R_0) and k_{off}^{app}. (**C**)

Determination of k_{off}^{max} at saturating mAb13 Fab concentration. k_{off}^{app} was fit to mAb13 Fab concentration using a dose response curve for the maximum off-rate at saturating mAb13 Fab concentration to determine k_{off}^{max}. The mAb13 Fab concentration when the off-rate reaches half of the maximum, EC_{50}^{mAb13} was also determined. Experiments in panels A and B were carried out twice, first with 0, 2, 5, 10 mAb13 Fab for 120 s, and then with the conditions shown, with similar k_{off}^{app} values in each experiment. Errors are SE from nonlinear least square fits.

Figure 7. Ligand-binding kinetics of each integrin state. (A) Integrin α4β1 and α5β1 ensembles utilized in this study to measure ligand-interaction kinetics and equations to relate the apparent on- and off- rates with the on- and off-rates for each conformational state. **(B)** Conformational state populations in absence ligand and when saturably bound to ligand. Previously reported populations for integrins in the absence of ligand and their affinities for ligand were used with Eqs. S5-S10 in Figure 7–figure supplement 3B.to calculate the populations in saturating ligand of ligand-bound integrin states in each type of ensemble studied here. The population of intact α4β1 on Jurkat cell surface in absence of ligand was reported in Figure 4D of (Li & Springer, 2018); population of intact α5β1 on K562 cell surface and α5β1 ectodomain in absence of ligand was reported in Figure 7 and Figure 4, respectively, in (Li *et al.*, 2017). The fold-difference in ligand binding affinity for the open and closed states that was used to calculate the populations for the ligand-saturated states is described in Figure 7–figure supplement 3. **(C)** Values of k_{on} and k_{off} for conformational states of four integrin-ligand pairs. As discussed in the text and Methods, kinetic measurements on the EO state and the extended and basal ensembles were used with equations in panel A to calculate kinetics of the BC and EC states. The errors for directly measured values were fitting errors from non-linear least square fit; the errors for calculated BC and EC values were propagated. [a]: Intrinsic rates of EO state was from measurements in presence of HUTS4 & 9EG7 Fabs in Figs. 2-4, and intrinsic rates for BC and EC states were calculated with Eqs. 1-4 in panel A. [b]: From previous equilibrium measurements described in the legends for Figure 2 and Figure 3. [c]: Calculated as shown from the product of equilibrium K_d and k_{on}. **(D)** Comparison of Asp-binding pocket in the open state (PDB: 3ze2 chains C+D) and closed state (PDB: 3zdy chains C+D) of integrin αIIBβ3 (Zhu *et al.*, 2013). The pocket in the β3 βI domain is shown with backbone and nearby sidechains in blue stick and blue dot surfaces and the MIDAS Mg^{2+} ion as a silver sphere. The ligand backbone loop is shown in yellow and its sidechain in stick with yellow carbons and red carboxyl oxygens. The Asp sidechain Cβ carbon and carboxyl oxygens are shown as yellow and red dot surfaces, respectively.

Figure 7–figure supplement 3. Ligand-interaction kinetics of integrin ensembles. (A) Reaction scheme showing two linked thermodynamic cycles. (B) Equations relating thermodynamic parameters and ligand-binding kinetics for reactions in Panel A. Equations S8-S10 are based on thermodynamic cycles for ligand binding and conformational change shown in Panel A. (C) Population of each state in absence of ligand and in presence of saturating concentration of ligand for selected integrin α4β1 and integrin α5β1 preparations. Population of each state in absence of ligand was reported in previous publications (Li & Springer, 2018; Li *et al.*, 2017). Specifically, data for intact α4β1 on cells were determined in Figure 4, and data for α4β1 unclasped ectodomains and headpiece were determined in Figure 3 in (Li & Springer, 2018). Data for intact α5β1 on cells were determined in Figure 7, data for α5β1 ectodomains and headpiece were determined in Figure 5 and Figure 6, respectively, in (Li *et al.*, 2017). Population of each state in ligand-bound forms are calculated from Eqs. S5-S10 shown in panel B. In Eqs. S8-S10, the ratios are used of intrinsic affinities of the EO state to the BC and EC states. For integrin α4β1, the ratios were averaged to 729±211 from six α4β1 preparations shown in the table (Li & Springer, 2018); for integrin α5β1, ratios were averaged to 3106 ±1689 from eight soluble α5β1 preparations, including the affinities of cRGD peptide for six ectodomain preparations either clasped or unclasped and with three different N-glycosylation forms (Figure 5), the affinities of cRGD peptide for highmannose headpiece and semi-truncated ectodomain

(Figure 6C), as well as affinity of Fn39-10 to unclasped ectodomain with high mannose N-glycans (Figure 4D) (Li *et al.*, 2017).

References

Akiyama SK, Yamada SS, Chen WT, Yamada KM (1989) Analysis of fibronectin receptor function with monoclonal antibodies: Roles in cell adhesion, migration, matrix assembly, and cytoskeletal organization. *J Cell Biol* 109: 863-875

Alon R, Dustin ML (2007) Force as a Facilitator of Integrin Conformational Changes during Leukocyte Arrest on Blood Vessels and Antigen-Presenting Cells. *Immunity* 26: 17-27

Alsallaq R, Zhou HX (2008) Electrostatic rate enhancement and transient complex of protein-protein association. *Proteins* 71: 320-335

Arimori T, Miyazaki N, Mihara E, Takizawa M, Taniguchi Y, Cabanas C, Sekiguchi K, Takagi J (2021) Structural mechanism of laminin recognition by integrin. *Nat Commun* 12: 4012

Astrof NS, Salas A, Shimaoka M, Chen JF, Springer TA (2006) Importance of force linkage in mechanochemistry of adhesion receptors. *Biochemistry* 45: 15020-15028

Bazzoni G, Shih D-T, Buck CA, Hemler MA (1995) Monoclonal antibody 9EG7 defines a novel β1 integrin epitope induced by soluble ligand and manganese, but inhibited by calcium. *J Biol Chem* 270: 25570-25577

Bouvard D, Pouwels J, De Franceschi N, Ivaska J (2013) Integrin inactivators: balancing cellular functions in vitro and in vivo. *Nat Rev Mol Cell Biol* 14: 430-442

Chigaev A, Blenc AM, Braaten JV, Kumaraswamy N, Kepley CL, Andrews RP, Oliver JM, Edwards BS, Prossnitz ER, Larson RS *et al* (2001) Real-time analysis of the affinity regulation of α4-integrin: the physiologically activated receptor is intermediate in affinity between resting and Mn^{2+} or antibody activation. *J Biol Chem* 276: 48670-48678

Clark K, Pankov R, Travis MA, Askari JA, Mould AP, Craig SE, Newham P, Yamada KM, Humphries MJ (2005) A specific α5β1-integrin conformation promotes directional integrin translocation and fibronectin matrix formation. *J Cell Sci* 118: 291-300

DeVree BT, Mahoney JP, Velez-Ruiz GA, Rasmussen SG, Kuszak AJ, Edwald E, Fung JJ, Manglik A, Masureel M, Du Y *et al* (2016) Allosteric coupling from G protein to the agonist-binding pocket in GPCRs. *Nature* 535: 182-186

Dong X, Zhao B, Iacob RE, Zhu J, Koksal AC, Lu C, Engen JR, Springer TA (2017) Force interacts with macromolecular structure in activation of TGF-β. *Nature* 542: 55-59

Dong X, Zhao B, Lin FY, Lu C, Rogers BN, Springer TA (2018) High integrin αVβ6 affinity reached by hybrid domain deletion slows ligand-binding on-rate. *Proc Natl Acad Sci U S A* 115: E1429-E1436

Dustin ML, Springer TA (1989) T cell receptor cross-linking transiently stimulates adhesiveness through LFA-1. *Nature* 341: 619-624

Galbraith CG, Yamada KM, Galbraith JA (2007) Polymerizing actin fibers position integrins primed to probe for adhesion sites. *Science* 315: 992-995

Hynes RO (1992) Integrins: versatility, modulation, and signaling in cell adhesion. *Cell* 69: 11-25

773 Iwamoto DV, Calderwood DA (2015) Regulation of integrin-mediated adhesions. *Curr Opin Cell*
774 *Biol* 36: 41-47

775 Kim C, Ye F, Ginsberg MH (2011) Regulation of integrin activation. *Annu Rev Cell Dev Biol* 27:
776 321-345

777 Kiosses WB, Shattil SJ, Pampori N, Schwartz MA (2001) Rac recruits high affinity integrin aVb3
778 to lamellipodia in endothelial cell migration. *Nat Cell Biol* 3: 316-320

779 Kokkoli E, Ochsenhirt SE, Tirrell M (2004) Collective and single-molecule interactions of α5β1
780 integrins. *Langmuir* 20: 2397-2404

781 Kuriyan JK, B.; Wemmer, D. (2012) The Molecules of Life: Physical and Chemical Principles. In:
782 Garland Science:

783 Lau TL, Kim C, Ginsberg MH, Ulmer TS (2009) The structure of the integrin αIIbβ3
784 transmembrane complex explains integrin transmembrane signalling. *EMBO J* 9: 1351-1361

785 Legate KR, Fassler R (2009) Mechanisms that regulate adaptor binding to β-integrin
786 cytoplasmic tails. *J Cell Sci* 122: 187-198

787 Li J, Springer TA (2017) Integrin extension enables ultrasensitive regulation by cytoskeletal
788 force. *Proc Natl Acad Sci U S A* 114: 4685-4690

789 Li J, Springer TA (2018) Energy landscape differences among integrins establish the framework
790 for understanding activation. *J Cell Biol* 217: 397-412

791 Li J, Su Y, Xia W, Qin Y, Humphries MJ, Vestweber D, Cabanas C, Lu C, Springer TA (2017)
792 Conformational equilibria and intrinsic affinities define integrin activation. *EMBO J* 36: 629-645

793 Luo BH, Carman CV, Springer TA (2007) Structural basis of integrin regulation and signaling.
794 *Annu Rev Immunol* 25: 619-647

795 Luque A, Gomez M, Puzon W, Takada Y, Sanchez-Madrid F, Cabanas C (1996) Activated
796 conformations of very late activation integrins detected by a group of antibodies (HUTS) specific
797 for a novel regulatory region (355-425) of the common β1 chain. *J Biol Chem* 271: 11067-11075

798 Moore TI, Aaron J, Chew TL, Springer TA (2018) Measuring integrin conformational change on
799 the cell surface with super-resolution microscopy. *Cell Rep* 22: 1903-1912

800 Mould AP, Askari JA, Byron A, Takada Y, Jowitt TA, Humphries MJ (2016) Ligand-induced
801 Epitope Masking: Dissociation of integrin α5β1-fibronectin complexes only by monoclonal
802 antibodies with an allosteric mode of action. *J Biol Chem* 291: 20993-21007

803 Mould AP, Craig SE, Byron SK, Humphries MJ, Jowitt TA (2014) Disruption of integrin-
804 fibronectin complexes by allosteric but not ligand-mimetic inhibitors. *Biochem J* 464: 301-313

805 Mould AP, Garratt AN, Askari JA, Akiyama SK, Humphries MJ (1995) Identification of a novel
806 anti-integrin monoclonal antibody that recognises a ligand-induced binding site epitope on the
807 β1 subunit. *FEBS Lett* 363: 118-122

808 Mould AP, Travis MA, Barton SJ, Hamilton JA, Askari JA, Craig SE, Macdonald PR, Kammerer
809 RA, Buckley PA, Humphries MJ (2005) Evidence that monoclonal antibodies directed against

the integrin β subunit plexin/semaphorin/integrin domain stimulate function by inducing receptor extension. *J Biol Chem* 280: 4238-4246

Nagae M, Re S, Mihara E, Nogi T, Sugita Y, Takagi J (2012) Crystal structure of $\alpha_5\beta_1$ integrin ectodomain: Atomic details of the fibronectin receptor. *J Cell Biol* 197: 131-140

Nordenfelt P, Elliott HL, Springer TA (2016) Coordinated integrin activation by actin-dependent force during T-cell migration. *Nat Commun* 7: 13119

Nordenfelt P, Moore TI, Mehta SB, Kalappurakkal JM, Swaminathan V, Koga N, Lambert TJ, Baker D, Waters JC, Oldenbourg R *et al* (2017) Direction of actin flow dictates integrin LFA-1 orientation during leukocyte migration. *Nat Commun* 8: 2047

Park YK, Goda Y (2016) Integrins in synapse regulation. *Nat Rev Neurosci* 17: 745-756

Phan UT, Waldron TT, Springer TA (2006) Remodeling of the lectin/EGF-like interface in P- and L-selectin increases adhesiveness and shear resistance under hydrodynamic force. *Nat Immunol* 7: 883-889

Sanchez-Madrid F, Krensky AM, Ware CF, Robbins E, Strominger JL, Burakoff SJ, Springer TA (1982) Three distinct antigens associated with human T lymphocyte-mediated cytolysis: LFA-1, LFA-2, and LFA-3. *Proc Natl Acad Sci U S A* 79: 7489-7493

Schumacher S, Dedden D, Nunez RV, Matoba K, Takagi J, Biertumpfel C, Mizuno N (2021) Structural insights into integrin α5β1 opening by fibronectin ligand. *Sci Adv* 7

Schürpf T, Springer TA (2011) Regulation of integrin affinity on cell surfaces. *EMBO J* 30: 4712-4727

Springer TA (1990) Adhesion receptors of the immune system. *Nature* 346: 425-433

Su Y, Xia W, Li J, Walz T, Humphries MJ, Vestweber D, Cabañas C, Lu C, Springer TA (2016) Relating conformation to function in integrin α5β1. *Proc Natl Acad Sci U S A* 113: E3872-3881

Sun Z, Costell M, Fassler R (2019) Integrin activation by talin, kindlin and mechanical forces. *Nat Cell Biol* 21: 25-31

Sun Z, Guo SS, Fassler R (2016) Integrin-mediated mechanotransduction. *J Cell Biol* 215: 445-456

Swaminathan V, Kalappurakkal JM, Mehta SB, Nordenfelt P, Moore TI, Koga N, Baker DA, Oldenbourg R, Tani T, Mayor S *et al* (2017) Actin retrograde flow actively aligns and orients ligand-engaged integrins in focal adhesions. *Proc Natl Acad Sci U S A* 114: 10648-10653

Takagi J, Erickson HP, Springer TA (2001) C-terminal opening mimics "inside-out" activation of integrin $\alpha_5\beta_1$. *Nat Struct Biol* 8: 412-416

Takagi J, Strokovich K, Springer TA, Walz T (2003) Structure of integrin α5β1 in complex with fibronectin. *EMBO J* 22: 4607-4615

Wallner J, Lhota G, Jeschek D, Mader A, Vorauer-Uhl K (2013) Application of Bio-Layer Interferometry for the analysis of protein/liposome interactions. *J Pharm Biomed Anal* 72: 150-154

847 Wei H, Mo J, Tao L, Russell RJ, Tymiak AA, Chen G, Iacob RE, Engen JR (2014)
848 Hydrogen/deuterium exchange mass spectrometry for probing higher order structure of protein
849 therapeutics: methodology and applications. *Drug Discov Today* 19: 95-102

850 Xia W, Springer TA (2014) Metal ion and ligand binding of integrin $\alpha_5\beta_1$. *Proc Natl Acad Sci U S*
851 *A* 111: 17863-17868

852 Xiao T, Takagi J, Wang J-H, Coller BS, Springer TA (2004) Structural basis for allostery in
853 integrins and binding of fibrinogen-mimetic therapeutics. *Nature* 432: 59-67

854 Yakovenko OT, V.; Sokurenko, E.V.; Thomas, W.E.. (2015) Inactive conformation enhances
855 binding function in physiological conditions. *Proc Natl Acad Sci USA* 112: 9884-9889

856 Yu Y, Schurpf T, Springer TA (2013) How natalizumab binds and antagonizes α4 integrins. *J*
857 *Biol Chem* 288: 32314-32325

858 Zhu J, Luo BH, Barth P, Schonbrun J, Baker D, Springer TA (2009) The structure of a receptor
859 with two associating transmembrane domains on the cell surface: integrin αIIbβ3. *Mol Cell* 34:
860 234-249

861 Zhu J, Luo BH, Xiao T, Zhang C, Nishida N, Springer TA (2008) Structure of a complete integrin
862 ectodomain in a physiologic resting state and activation and deactivation by applied forces. *Mol*
863 *Cell* 32: 849-861

864 Zhu J, Zhu J, Springer TA (2013) Complete integrin headpiece opening in eight steps. *J Cell*
865 *Biol* 201: 1053-1068

866

A. Integrin conformational ensemble

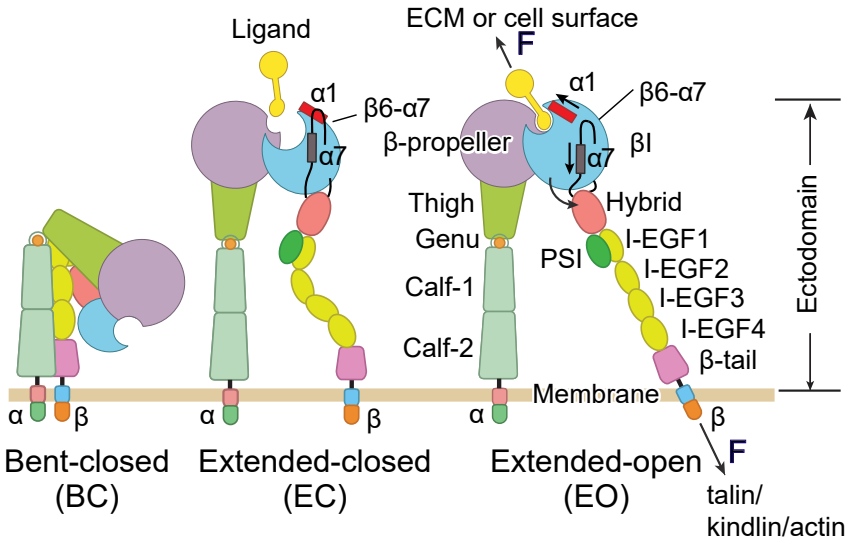

B. Integrin ligand binding

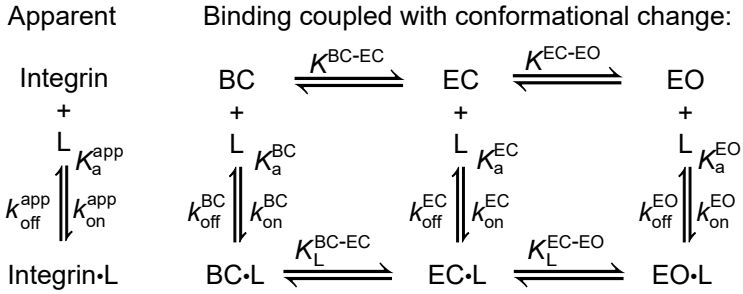

C. Fabs against β1 subunit or α5 subunit used in this study

Name	Domain	Conformational specificity
8E3	PSI	EC + EO
9EG7	I-EGF2	EC + EO
SNAKA51	Calf-1/Calf-2	EC + EO
HUTS4	hybrid	EO
12G10	βI	EO
mAb13	βI	BC + EC

Figure 1. Integrin conformational ensemble and conformational specific Fabs used to stabilize a defined ensemble.

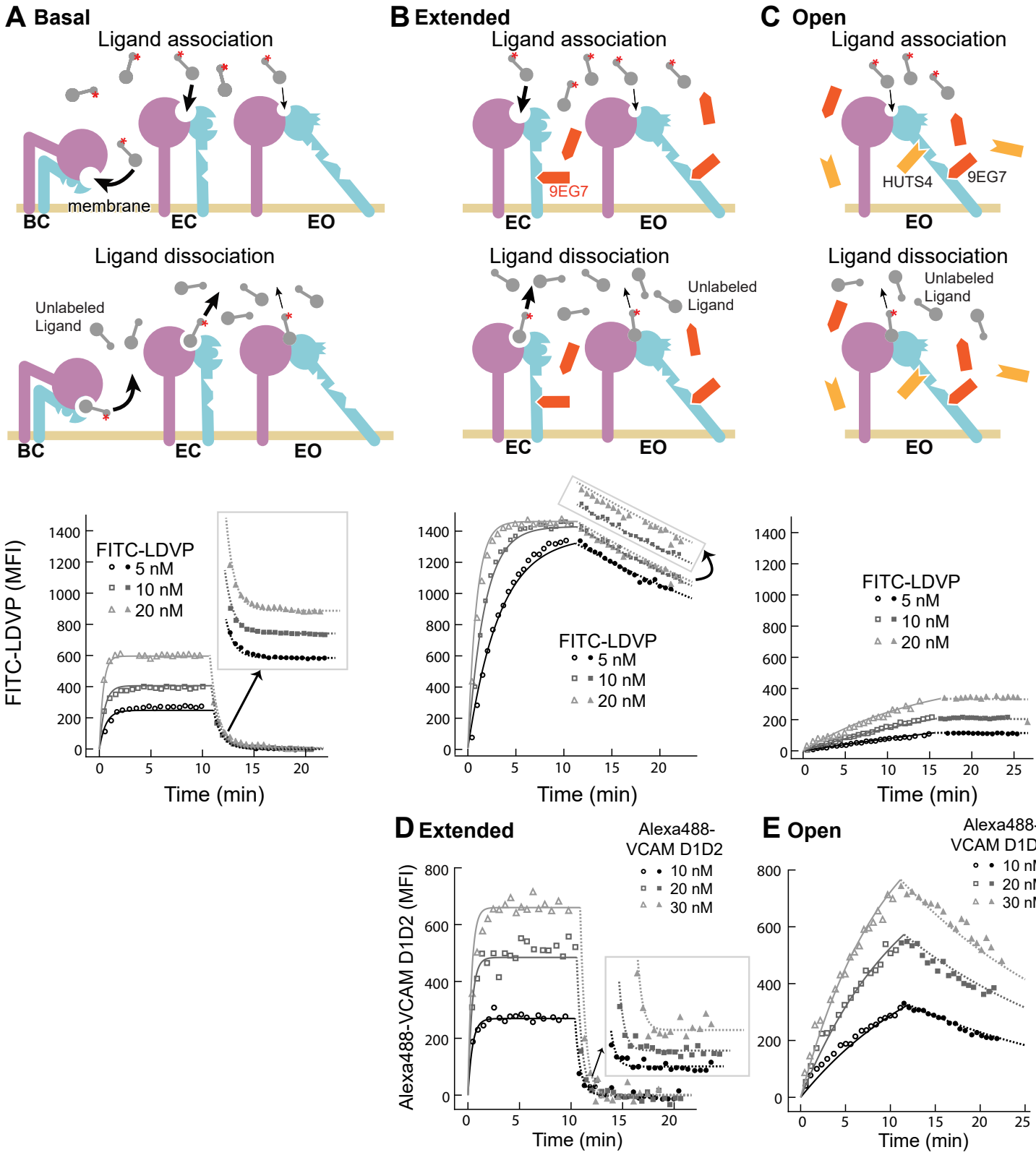

F FITC-LDVP and Alexa488-VCAM D1D2 binding to intact α4β1 on Jurkat cells

Condition	FITC-LDVP				Alexa488-VCAM D1D2			
	k_{on}^{app} (10^4 $M^{-1}s^{-1}$)	k_{off}^{app} (10^{-3} s^{-1})	$k_{off}^{app}/k_{on}^{app}$ (nM)	K_d (nM)	k_{on}^{app} (10^4 $M^{-1}s^{-1}$)	k_{off}^{app} (10^{-3} s^{-1})	$k_{off}^{app}/k_{on}^{app}$ (nM)	K_d (nM)
Basal	120±10	19±3	15.8±2.8	15.0±2.1				
Extended	87±8	0.36±0.11	0.41±0.13	0.25±0.05	43±6	34±2	79±13	160±40
Open	5.6±0.2	0.021±0.018	0.38±0.34	0.18±0.02	3.4±0.2	0.72±0.02	21±1	30±4

Figure 2. Binding kinetics of ligands to intact α4β1 on Jurkat cells.

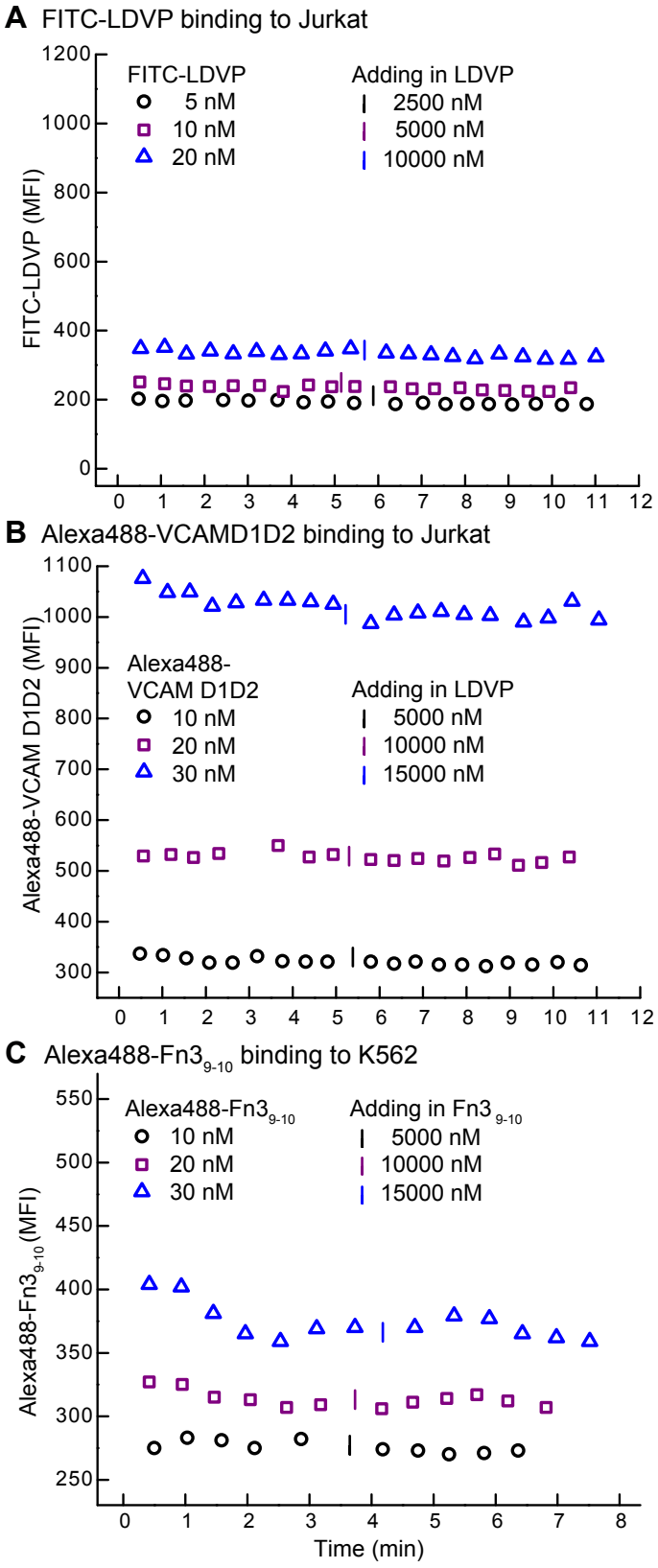

Figure 2, 3–figure supplement 1. Background binding of fluorescent ligands in presence of 10 mM EDTA.

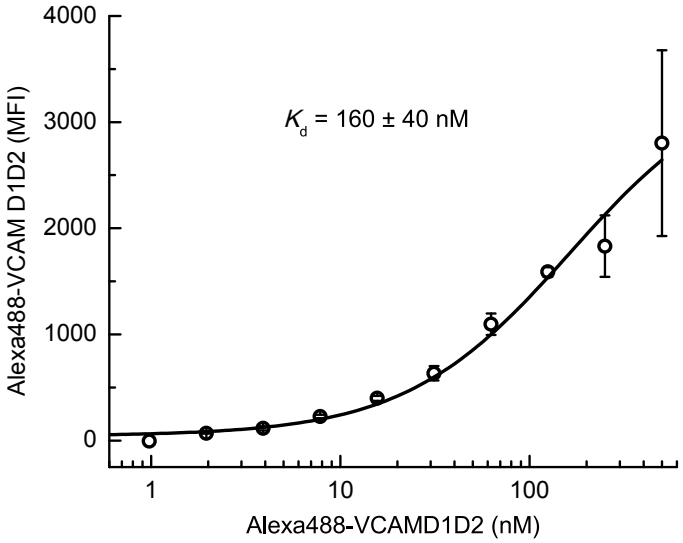

Figure 2–figure supplement 2. Binding of Alexa488-VCAM D1D2 to Jurkat cells under extension-stabilizing Fabs monitored by FACS.

A **Extended**

Ligand association

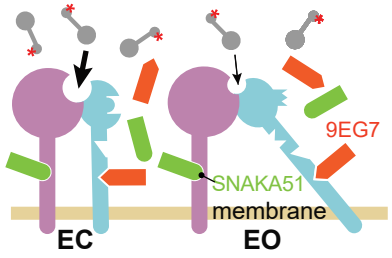

Ligand dissociation

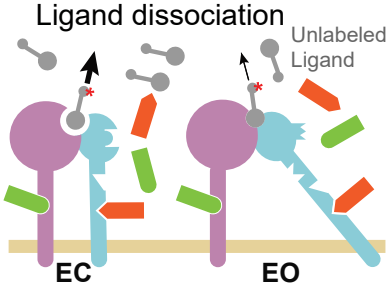

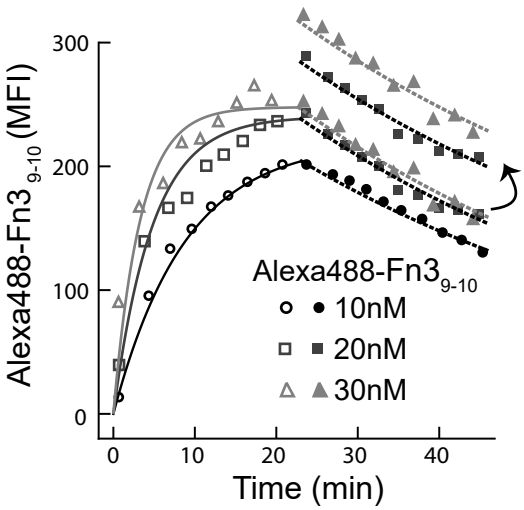

B **Open**

Ligand association

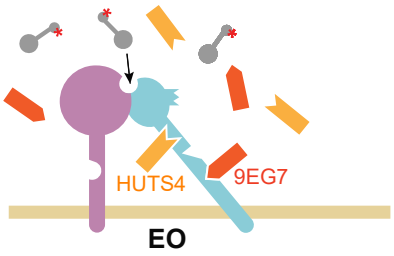

Ligand dissociation

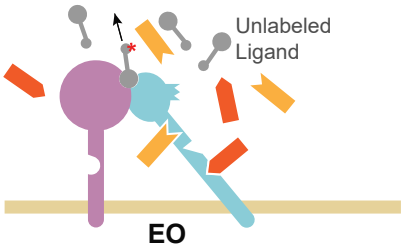

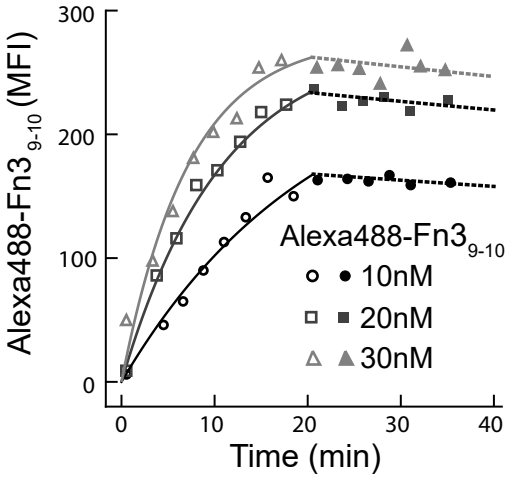

C Alexa488-Fn3$_{9\text{-}10}$ binding to intact α5β1 on K562 cells

Condition	k_{on}^{app} (10^4 $M^{-1}s^{-1}$)	k_{off}^{app} (10^{-3} s^{-1})	$k_{off}^{app}/k_{on}^{app}$ (nM)	K_d (nM)
Extended	15.8±0.7	0.32±0.02	2.0±0.2	1.9±0.1
Open	7.5±0.3	0.052±0.021	0.7±0.3	1.3±0.1

Figure 3. Binding kinetics of Alexa488-Fn3$_{9\text{-}10}$ to α5β1 on K562 cells.

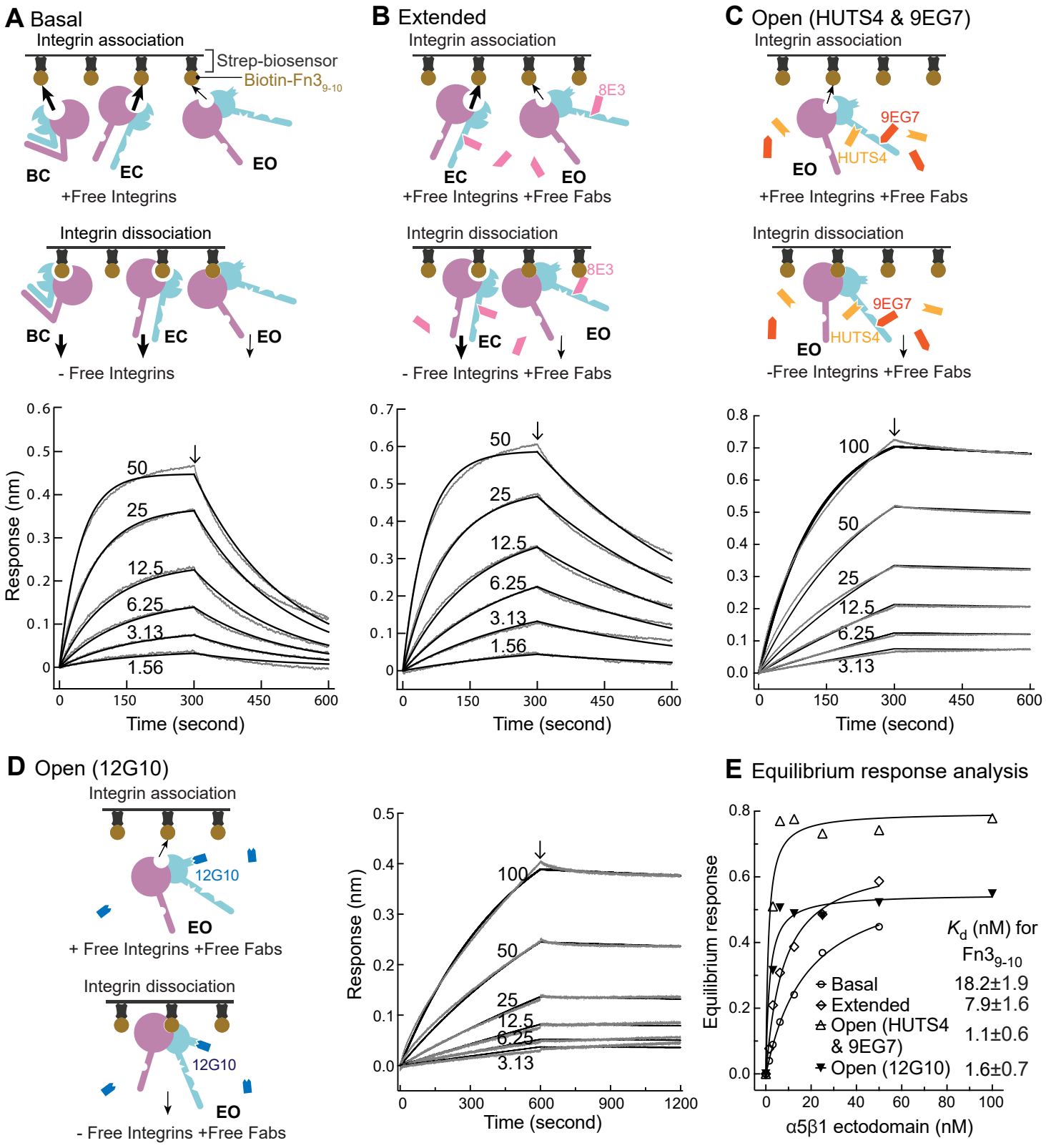

F α5β1 ectodomain binding to biotin-Fn3$_{9-10}$

	k_{on}^{app} (10^4 $M^{-1}s^{-1}$)	k_{off}^{app} (10^{-3} s^{-1})	$k_{off}^{app}/k_{on}^{app}$ (nM)	K_d (nM)
Basal	33±1	5.0±0.1	14.9±0.1	18.2±1.9
Extended	33±1	2.3±0.1	7.0±0.1	7.9±1.6
Open (HUTS4&9EG7)	7.9±0.2*	0.093±0.013*	1.2±0.2	1.1±0.6
Open (12G10)	1.95±0.05*	0.047±0.008*	2.4±0.1	1.6±0.7

Figure 4. Binding kinetics of α5β1 ectodomain to Fn3$_{9-10}$

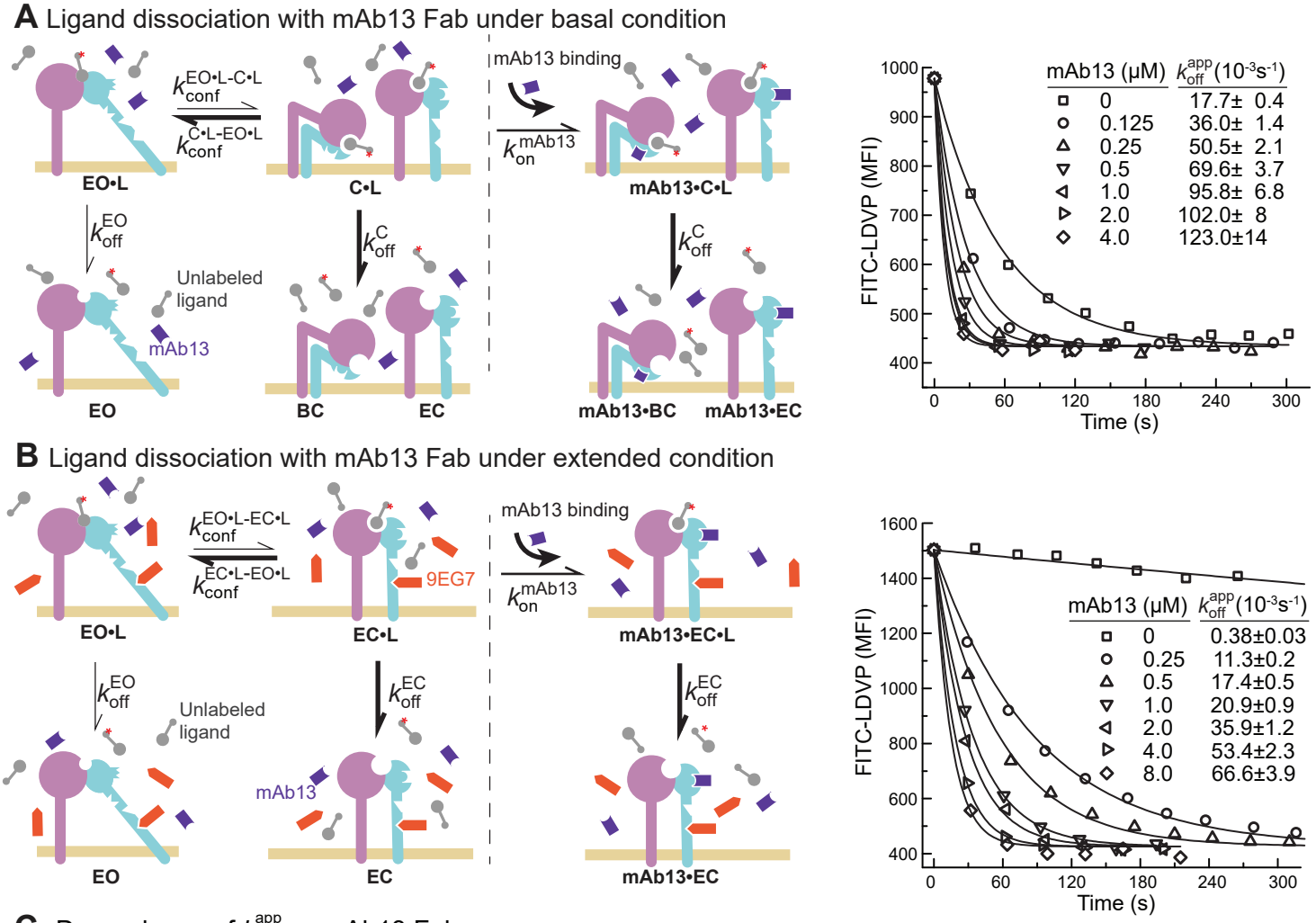

Figure 5. Dissociation of FITC-LDVP from intact α4 β1 in presence of closure-stabilizing Fab.

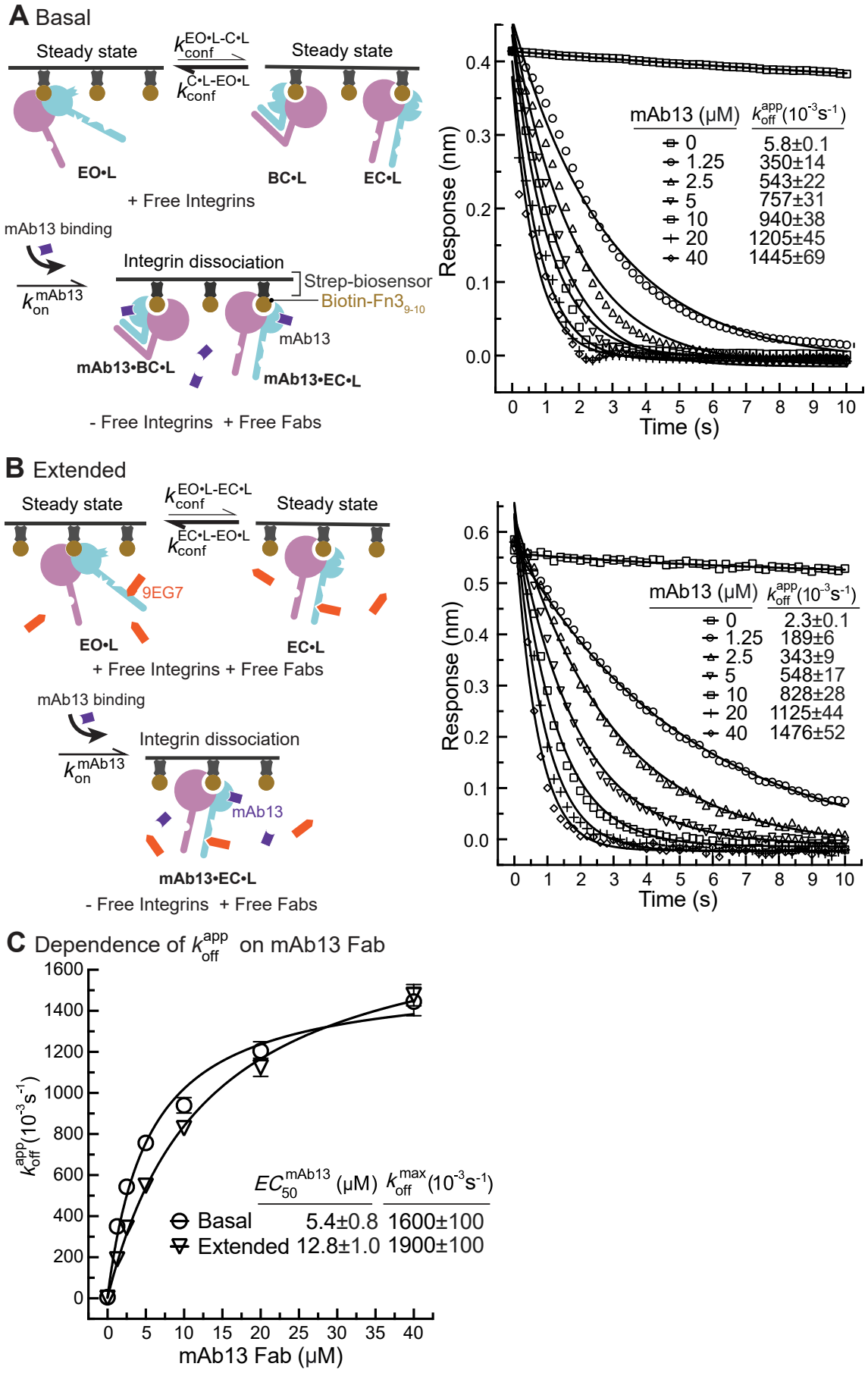

Figure 6. Dissociation of α5β1 ectodomain from biotin-Fn3$_{9-10}$ in presence of closure-stabilizing Fab.

A Strategy for determining intrinsic on- and off rates of each integrin state

Condition	States present in the ensemble	k_{on}^{app} and k_{off}^{app} for ligand
Open	EO	k_{on}^{EO}
	EO•L	k_{off}^{EO}
Extended	EC, EO	$k_{on}^{app(EC+EO)} \approx \frac{P^{EC}}{P^{EC}+P^{EO}} k_{on}^{EC} + \frac{P^{EO}}{P^{EC}+P^{EO}} k_{on}^{EO}$ (Eq.1)
	EC•L, EO•L	$k_{off}^{app(EC+EO)} \approx \frac{P^{EC•L}}{P^{EC•L}+P^{EO•L}} k_{off}^{EC} + \frac{P^{EO•L}}{P^{EC•L}+P^{EO•L}} k_{off}^{EO}$ (Eq.2)
Basal	BC, EC, EO	$k_{on}^{app(BC+EC+EO)} \approx P^{BC} k_{on}^{BC} + P^{EC} k_{on}^{EC} + P^{EO} k_{on}^{EO}$ (Eq.3)
	BC•L, EC•L, EO•L	$k_{off}^{app(BC+EC+EO)} \approx P^{BC•L} k_{off}^{BC} + P^{EC•L} k_{off}^{EC} + P^{EO•L} k_{off}^{EO}$ (Eq.4)

B Conformational state populations (%) in absence of ligand and when bound to ligand at saturating concentrations

Ligand bound	Ensemble	intact α4β1-Jurkat			intact α5β1-K562			α5β1-ectodomain		
		BC	EC	EO	BC	EC	EO	BC	EC	EO
-	Basal	98.5	0.4	1.1	99.84	0.05	0.11	64.3	31.1	4.6
-	Extended	0	28	72	0	30	70	0	87.1	12.9
-	Open	0	0	100	0	0	100	0	0	100
+	Basal	10.9	0.04	89.0	22.6	0.01	77.4	0.5	0.2	99.3
+	Extended	0	0.05	99.95	0	0.01	99.99	0	0.2	99.8
+	Open	0	0	100	0	0	100	0	0	100

C Intrinsic on- and off- rates of each integrin state for ligand

		BC	EC	EO
Intact α4β1 for LDVP	k_{on} ($10^4 M^{-1}s^{-1}$)[a]	120±20	300±170	5.6±0.2
	k_{off} ($10^{-3}s^{-1}$)[a]	170±60	640±590	0.021±0.018
	K_d (nM)[b]	130±40	130±40	0.18±0.02
	$k_{off} = K_d * k_{on}$ ($10^{-3}s^{-1}$)[c]	160±60	390±250	0.010±0.001
Intact α4β1 for VCAM D1D2	k_{on} ($10^4 M^{-1}s^{-1}$)[a]		150±90	3.4±0.2
	k_{off} ($10^{-3}s^{-1}$)[a]		57000±23000	0.72±0.02
	K_d (nM)[b]		22000±7000	30±4
	$k_{off} = K_d * k_{on}$ ($10^{-3}s^{-1}$)[c]		33000±22000	1.0±0.1
Intact α5β1 for $Fn3_{9-10}$	k_{on} ($10^4 M^{-1}s^{-1}$)[a]		35±6	7.5±0.3
	k_{off} ($10^{-3}s^{-1}$)[a]		1900±1200	0.052±0.021
	K_d (nM)[b]		4000±2100	1.3±0.1
	$k_{off} = K_d * k_{on}$ ($10^{-3}s^{-1}$)[c]		1400±800	0.098±0.001
α5β1 ecto for $Fn3_{9-10}$	k_{on} ($10^4 M^{-1}s^{-1}$)[a]	34±2	37±2	7.9±0.2
	k_{off} ($10^{-3}s^{-1}$)[a]	740±400	1000±600	0.093±0.013
	K_d (nM)[b]	3400±2600	3400±2600	1.1±0.6
	$k_{off} = K_d * k_{on}$ ($10^{-3}s^{-1}$)[c]	1200±900	1300±1000	0.085±0.046

D Asp-binding pocket is tighter in the open state

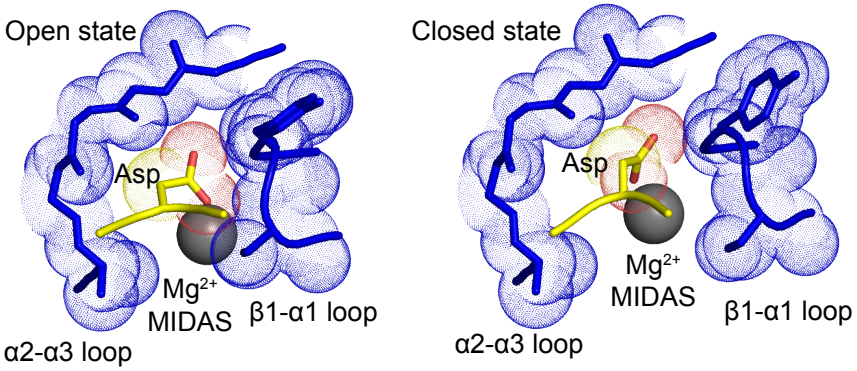

Figure 7. Ligand-binding kinetics of each integrin state.

A Binding coupled with conformational change:

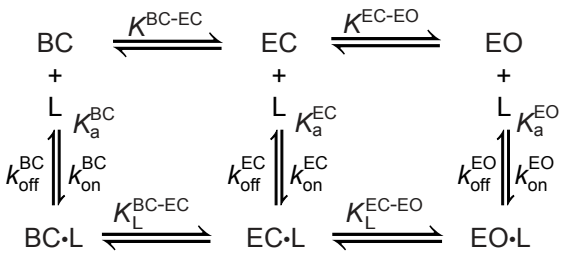

B Ligand binding kinetics and thermodynamics

$$\frac{k_{on}^{app}}{k_{off}^{app}} = K_a^{app} = \frac{[\text{Integrin•L}]}{[\text{Integrin}][L]} \quad \text{(Eq.S1)}$$

$$\frac{k_{on}^{BC}}{k_{off}^{BC}} = K_a^{BC} = \frac{[BC•L]}{[BC][L]} \quad \text{(Eq.S2)}$$

$$\frac{k_{on}^{EC}}{k_{off}^{EC}} = K_a^{EC} = \frac{[EC•L]}{[EC][L]} \quad \text{(Eq.S3)}$$

$$\frac{k_{on}^{EO}}{k_{off}^{EO}} = K_a^{EO} = \frac{[EO•L]}{[EO][L]} \quad \text{(Eq.S4)}$$

$$K^{BC\text{-}EC} = \frac{P^{EC}}{P^{BC}} \quad \text{(Eq.S5)}$$

$$K^{EC\text{-}EO} = \frac{P^{EO}}{P^{EC}} \quad \text{(Eq.S6)}$$

$$K^{BC\text{-}EO} = \frac{P^{EO}}{P^{BC}} \quad \text{(Eq.S7)}$$

$$K_L^{BC\text{-}EC} = \frac{P^{EC•L}}{P^{BC•L}} = K^{BC\text{-}EC}\frac{K_a^{EC}}{K_a^{BC}} \quad \text{(Eq.S8)}$$

$$K_L^{EC\text{-}EO} = \frac{P^{EO•L}}{P^{EC•L}} = K^{EC\text{-}EO}\frac{K_a^{EO}}{K_a^{EC}} \quad \text{(Eq.S9)}$$

$$K_L^{BC\text{-}EO} = \frac{P^{EO•L}}{P^{BC•L}} = K^{BC\text{-}EO}\frac{K_a^{EO}}{K_a^{BC}} \quad \text{(Eq.S10)}$$

C Basal conformational state populations (%) of integrin preparations, with incated N-glycan form and presence of C-terminal clasped or not for the soluble ectodomain preparations, in absence of ligand and when bound to ligand at saturating concentrations

Ligand bound	intact α4β1-Jurkat complex			intact α4β1-Thp1 complex			intact α4β1-KA4 complex			α4β1-ectodomain complex, unclasped			α4β1-ectodomain high-mannose, unclasped			α4β1-headpiece high-mannose	
	BC	EC	EO	BC	EC	EO	BC	EC	EO	BC	EC	EO	BC	EC	EO	C	O
-	98.5	0.4	1.1	99.3	0.3	0.4	97.7	0.9	1.4	21.8	43.5	34.7	27.5	63.5	9.0	97.7	2.3
+	10.9	0.04	89.0	25.4	0.08	74.5	8.7	0.08	91.2	0.08	0.20	99.7	0.3	1.0	98.6	5.5	94.5

Ligand bound	intact α5β1-Jurkat complex			intact α5β1-K562 complex			α5β1-ectodomain complex, clasped			α5β1-ectodomain complex, unclasped		
	BC	EC	EO	BC	EC	EO	BC	EC	EO	BC	EC	EO
-	99.82	0.01	0.17	99.84	0.05	0.11	85.1	4.2	10.8	52.2	17.1	30.7
+	15.9	0.002	84.1	22.6	0.01	77.4	0.25	0.01	99.7	0.05	0.03	99.9

Ligand bound	α5β1-ectodomain high-mannose, clasped			α5β1-ectodomain high-mannose, unclasped			α5β1-ectodomain shaved, clasped			α5β1-ectodomain shaved, unclasped			α5β1-headpiece high-mannose	
	BC	EC	EO	BC	EC	EO	BC	EC	EO	BC	EC	EO	C	O
-	94.9	3.6	1.5	64.3	31.1	4.6	90.5	8.6	0.9	59.3	38.8	2.0	99.97	0.03
+	2.0	0.08	97.9	0.5	0.2	99.3	3.1	0.3	96.6	0.9	0.6	98.4	51.8	48.2

Figure 7–figure supplement 3. Ligand-interaction kinetics of integrin ensembles.